

NASA/TM-2000-208785
AFDD/TR-99-A-001



Preliminary Study of a Model Rotor in Descent

K. W. McAlister, C. Tung, D. L. Sharpe, S. Huang, and E. M. Hendley

November 2000

The NASA STI Program Office . . . in Profile

Since its founding, NASA has been dedicated to the advancement of aeronautics and space science. The NASA Scientific and Technical Information (STI) Program Office plays a key part in helping NASA maintain this important role.

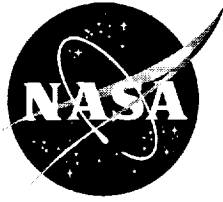
The NASA STI Program Office is operated by Langley Research Center, the Lead Center for NASA's scientific and technical information. The NASA STI Program Office provides access to the NASA STI Database, the largest collection of aeronautical and space science STI in the world. The Program Office is also NASA's institutional mechanism for disseminating the results of its research and development activities. These results are published by NASA in the NASA STI Report Series, which includes the following report types:

- **TECHNICAL PUBLICATION.** Reports of completed research or a major significant phase of research that present the results of NASA programs and include extensive data or theoretical analysis. Includes compilations of significant scientific and technical data and information deemed to be of continuing reference value. NASA's counterpart of peer-reviewed formal professional papers but has less stringent limitations on manuscript length and extent of graphic presentations.
- **TECHNICAL MEMORANDUM.** Scientific and technical findings that are preliminary or of specialized interest, e.g., quick release reports, working papers, and bibliographies that contain minimal annotation. Does not contain extensive analysis.
- **CONTRACTOR REPORT.** Scientific and technical findings by NASA-sponsored contractors and grantees.
- **CONFERENCE PUBLICATION.** Collected papers from scientific and technical conferences, symposia, seminars, or other meetings sponsored or cosponsored by NASA.
- **SPECIAL PUBLICATION.** Scientific, technical, or historical information from NASA programs, projects, and missions, often concerned with subjects having substantial public interest.
- **TECHNICAL TRANSLATION.** English-language translations of foreign scientific and technical material pertinent to NASA's mission.

Specialized services that complement the STI Program Office's diverse offerings include creating custom thesauri, building customized databases, organizing and publishing research results . . . even providing videos.

For more information about the NASA STI Program Office, see the following:

- Access the NASA STI Program Home Page at <http://www.sti.nasa.gov>
- E-mail your question via the Internet to help@sti.nasa.gov
- Fax your question to the NASA Access Help Desk at (301) 621-0134
- Telephone the NASA Access Help Desk at (301) 621-0390
- Write to:
NASA Access Help Desk
NASA Center for Aerospace Information
7121 Standard Drive
Hanover, MD 21076-1320



Preliminary Study of a Model Rotor in Descent

K. W. McAlister, C. Tung, D. L. Sharpe, S. Huang, and E. M. Hendley
Aeroflightdynamics Directorate
U.S. Army Aviation and Missile Command
Ames Research Center, Moffett Field, California

National Aeronautics and
Space Administration

Ames Research Center
Moffett Field, California 94035-1000

Available from:

NASA Center for AeroSpace Information
7121 Standard Drive
Hanover, MD 21076-1320
(301) 621-0390

National Technical Information Service
5285 Port Royal Road
Springfield, VA 22161
(703) 487-4650

Preliminary Study of a Model Rotor in Descent

K. W. MCALISTER, C. TUNG, D. L. SHARPE, S. HUANG, AND E. M. HENDLEY

*Aeroflightdynamics Directorate, U.S. Army Aviation and Missile Command
Ames Research Center*

Summary

Within a program designed to develop experimental techniques for measuring the trajectory and structure of vortices trailing from the tips of rotor blades, the present preliminary study focuses on a method for quantifying the trajectory of the trailing vortex during descent flight conditions. This study also presents rotor loads and blade surface pressures for a range of tip-path plane angles and Mach numbers. Blade pressures near the leading edge and along the outer radius are compared with data obtained on the same model rotor, but in open jet facilities. A triangulation procedure based on two directable laser-light sheets, each containing an embedded reference, proved effective in defining the spatial coordinates of the trailing vortex. When interrogating a cross section of the flow that contains several trailing vortices, the greatest clarity was found to result when the flow is uniformly seeded. Surface pressure responses during blade-vortex interactions appeared equally sensitive near the leading edge and along the outer portion of the blade, but diminished rapidly as the distance along the blade chord increased. The pressure response was virtually independent of whether the tip-path plane angle was obtained through shaft tilt or cyclic pitch. Although the shape and frequency of the pressure perturbations on the advancing blade during blade-vortex interaction are similar to those obtained in open-jet facilities, the angle of the tip-path plane may need to be lower than the range covered in this study.

Nomenclature

a	speed of sound
A₁	longitudinal cyclic pitch angle
B₁	lateral cyclic pitch angle
c	blade chord
C_p	pressure coefficient, $(p - p_s)/q_i$
ΔC_p	differential pressure coefficient, $(p_u - p_l)/q_i$
C_T	thrust coefficient, $thrust/\rho\pi\Omega^2 R^4$
M	Mach number, $(r\Omega + V_\infty \sin\psi)/a$
M_{at}	advancing tip Mach number, $(R\Omega + V_\infty)/a$

M_h	hover tip Mach number, $R\Omega/a$
p	blade pressure (either p_u or p_l)
p_l	blade pressure on lower surface
p_s	freestream static pressure
p_u	blade pressure on upper surface
q	freestream dynamic pressure, $\rho V_\infty^2/2$
q_l	local blade dynamic pressure, $1/2\rho(r\Omega + V_\infty \sin\psi)^2$
r	local radius along blade
R	blade radius at tip
Re	Reynolds number, cV_{at}/ν
V_{at}	advancing tip velocity, $R\Omega + V_\infty$
V_∞	freestream velocity
x	chordwise distance from leading edge of blade
α_{tp}	angle between freestream and tip-path plane
θ	blade pitch angle, $\theta = \theta_0 + A_1 \sin\psi + B_1 \cos\psi$
θ_0	collective pitch angle
μ	advance ratio, $V_\infty/R\Omega$
ν	fluid kinematic viscosity
ρ	fluid density
ψ	rotor blade azimuth
Ω	rotational speed of rotor

Introduction

Although the current civil helicopter has been used extensively because of its excellent hover and low-speed forward flight capability, the fleet continues to exhibit noise levels that are too high for widespread community acceptance. A major source of helicopter noise originates from the rotor blade cutting through its own wake. This phenomenon is known as blade-vortex interaction (BVI) noise and is most prominent when descending for a landing.

Many experimental studies have been performed over the last decade to investigate the BVI phenomenon. The experiments have ranged from full-scale flight tests (refs. 1 and 2) to model-scale tests (refs. 3–5). At lower advance ratios ($\mu < 0.2$), it was found that BVI noise can be scaled (refs. 6 and 7), suggesting that expensive flight tests can often be simulated by model rotor tests.

BVI events are highly impulsive. Specifically, rotor-blade acoustics are a function of surface-pressure fluctuations, which in turn are influenced by the geometry and composition of the trailing vortices within the rotor wake and with which the blades interact. Analytical methods for calculating rotor acoustics are dependent on an accurate description of the vortex wake (refs. 8 and 9). Reliable and detailed information of this sort is normally derived from experiments; however, reports of these measurements are rather sparse.

The most dominant feature characterizing the rotor wake is the tangle of vortices trailing from the tips of the rotor blades. Attempts to visualize the rotor wake in wind tunnels typically fall into two groups. One group depends on density variations in the flow that result from the low pressure near the center of the vortex. Schlieren and shadowgraph techniques (refs. 10–15) can image the resulting variation in air density, and therefore the vortex geometry. The other group relies on the induced flow around the vortex to entrain the particles that are deliberately injected into the stream. The particles are redistributed in a characteristic pattern that reveals the location of the vortex when illuminated with a laser light sheet (refs. 16–19). The wake geometry presented in reference 20, which features the locations of vortex segments at discrete azimuths, is a good example of wake data obtained in this fashion.

This present experimental study was undertaken to establish a technique for defining the wake geometry and structure of the trailing vortex, and to explore the possibility of complementing the acoustic measurements on model rotors performed in other facilities. The bridge between a wake study in one facility and an acoustic study in another facility would be the correlation of blade pressures in the two experiments. A model rotor experiment performed in another facility, which focused on acoustics and included blade pressure but lacked information about the wake geometry, was reported in reference 21. That test was conducted at high forward speed and for several BVI conditions on a model rotor in an open jet, anechoic test facility. In the present study a test is performed on the same model rotor, but in a closed test section and with the angle of the tip-path plane adjusted to replicate one of the BVI conditions in the open jet test. Aside from exploring the efficacy of

matching open and closed jet results, the long-range benefit from this effort is the development of techniques for measuring model rotor loads, wake geometry, blade deformation, and trailing vortex structure (core size and strength) during a BVI (descent) condition. This report contains the results from the first phase of this study (identified as *LoTuS*) and focuses on the rotor loads and the technique for measuring wake geometry.

Description of Experiment

Facility and Model

The test was conducted in the 7- by 10-Foot Wind Tunnel at Ames Research Center, using a 1/7-scale model of the AH-1/OLS rotor. The rotor consists of two blades, with a chord dimension of 4.09 in. and a span of 37.7 in. measured from the axis of rotation to the blade tip (fig. 1). The rotor disk was located approximately in the center of the test section, with the rotor diameter spanning about 63% of the width of the test section (fig. 2). Beginning at 25% radius, the twist of each blade was $-0.27^\circ/\text{in.}$, so that the total variation in geometric twist along the span was 7.55° . Collective pitch settings were referenced to the geometric pitch angle at 75% radius. Therefore, a collective pitch setting of zero means that the blade pitch was about 5.0° at the root (held fixed for locations $< R/4$) and -2.5° at the tip. The rotor hub has a built-in blade precone of 1.3° .

The blades were instrumented with surface pressure transducers and safety-of-flight gages. One blade contained 28 absolute pressure transducers (14 were located on the upper surface and 14 on the lower surface) and the other contained 18 differential pressure transducers (fig. 3). Calibrations were performed by applying a vacuum to each transducer, either individually for the differential transducers or collectively (using a cylindrical cuff) for the absolute transducers. Information related to flight safety was obtained by flap- and chord-bending gages mounted on the blade (fig. 4). The drag link used to adjust the blade sweep was instrumented with a strain gage that responded to the aerodynamic drag on the rotor, and as such, offered a redundant measurement of chord-wise bending. Depending on the sweep of the blade and the location of the center of mass of the blade, this gage could also be loaded by a centrifugal force induced moment. Strain gages were placed on the pitch horns that transmitted commands to the rotor blades. Reactions to these commands resulted in bending loads on these elements that were proportional to the pitching moments on the blades. A transducer (called the teeter pot) for measuring the angular tilt of the rotor was mounted on top

of the hub. The rotor operator monitored the signals from each of these gages.

The excitation and signal wires from the safety gages and pressure transducers were passed down through the shaft (fig. 5) and the junctions were secured with tape and string (fig. 6). The swashplate and related pitch controls are shown in figure 7. The rotor hub was mounted on the VSB-54 force and moment balance, and the rotor stand was attached to a plate to achieve a range of tip-path planes based on shaft tilt (fig. 8). The entire rotor assembly could be positioned in the streamwise direction (fig. 9) so that the rotor wake would be in the most optimum position for viewing through the test section windows (location established during model installation).

Based on microphone and blade pressure measurements collected in earlier tests (refs. 3 and 7), appreciable BVI noise was found to occur at several descent conditions (ref. 8). Considering one of these test conditions, $M_h = 0.664$ and $\mu = 0.164$ (Deutsch-Niederlandischer Windkanal (DNW) case number 10014), and given a freestream temperature of 58°F in the present test, the required tunnel and rotor speeds for the present test were calculated to be $V_\infty = 122$ fps ($q = 0.122$ psi) and $\Omega = 2250$ rpm. The corresponding advancing tip Mach and Reynolds numbers are $M_{at} = 0.77$ and $Re = 1.88 \times 10^6$ (advancing tip speed $V_{at} = 862$ fps).

Since the center of mass of each rotor blade was located aft of the feathering axis (aligned with the quarter chord), it was necessary to sweep the blades forward 1.2° to minimize steady chordwise bending due to centripetal force. The blades were strobed at 2/rev to verify that the blades were tracking. A blade sweep of 1.2° corresponds to a 0.19c movement of the tip. Stand accelerometers indicated any imbalance in the rotor system and lead weights were added as needed to the blade retention bolt.

Data Acquisition

Blade related instrumentation consisted of gages measuring load reactions (flap and chord bending) and gages measuring local surface pressure. These dynamic signals were conditionally sampled based on an encoder attached to the transmission and having a resolution of 1024 per revolution. A limited number of pressure transducers were selected based on their present working condition, the existence of archived electronic files from the DNW test, and presentations of their response during BVI in figures contained in references 8 and 22. These criteria resulted in the selection of 19 transducers (see table 1).

Table 1. Blade pressure transducers

ID	Type	r/R	x/c				
			0.03	0.08	0.15	0.35	0.5
1U	Absolute	0.97					
3L	Absolute	0.97					
4L	Absolute	0.97					
2U	Absolute	0.955					
3U	Absolute	0.955					
5U	Absolute	0.955					
8U	Absolute	0.955					
12U	Absolute	0.91					
9L	Absolute	0.9					
10L	Absolute	0.869					
16L	Absolute	0.74					
1D	Differential	0.955					
2D	Differential	0.955					
6D	Differential	0.864					
15D	Differential	0.8					
9D	Differential	0.75					
10D	Differential	0.75					
16D	Differential	0.7					
17D	Differential	0.6					

Wind tunnel related data consisting of freestream temperature and freestream static and dynamic pressures were recorded separately and later used in the calculation of dimensionless quantities such as Mach number, thrust coefficient, and pressure coefficient. Values for the longitudinal and lateral cyclic pitch, collective pitch, and shaft tilt were also recorded as part of the parameter set identifying the test conditions.

A strain gage bridge mounted on the flex coupling located between the transmission and the balance measured torque. The remainder of the rotor loads was obtained with the temperature compensated VSB-54 force balance. The allowable load limits are given in table 2.

Table 2. Allowable loads

Gage	ID	Max. allowable	Max. alternating
Normal 1	1	500 lb	200 lb
Normal 2	2	500 lb	200 lb
Side 1	3	500 lb	200 lb
Side 2	4	500 lb	200 lb
Axial 1	5	600 lb	240 lb
Axial 2	6	1400 lb	560 lb
Torque		510 ft-lb	

To account for interactions between the various balance gages, each force was calculated according to:

$$F_i = (V_i - Z_i) C_{ij}$$

Where F , V , Z , and C represent the resultant gage force, load voltage, zero-load voltage, and calibration constant, respectively. Each of the balance gages is referenced by the subscript "i" and the matrix of calibration constants is given in table 3.

The most important quantity measured by the rotor balance was the axial force. With this measurement the thrust coefficient was calculated and displayed in real time so that the collective pitch could be set to yield $C_T = 0.0054$ (the condition matching the DNW data). The procedure used to match the targeted DNW condition is outlined in figure 10. Although data were taken at lower rotor speeds, the DNW matching quantities were fixed at

$M_h = 0.664$ ($M_{at} = 0.77$), $\mu = 0.164$, and $C_T = 0.0054$.

Given the freestream temperature in the present test, the necessary rotor rpm and freestream velocity were calculated. Assuming the tip-path plane to be the only variable to be adjusted to account for the difference between an open and closed jet test, the angle of the tip-path plane was arbitrarily set (but within a few degrees of 1°) and some value for the collective pitch was selected. If the tip-path plane was to be established by shaft tilt (rather than with cyclic pitch), then the cyclic pitch was adjusted until the flapping was nulled. The axial force was examined to determine if the correct thrust coefficient had been achieved. If not, a new value for the collective pitch was set. Once the thrust coefficient had been matched, blade pressure data were recorded and compared with the DNW results. If the pressure did not match, a new value for the tip-path plane was set, and the procedure was repeated.

The procedure for quantifying the wake geometry was based on flow visualization. The technique depended on the flow being properly seeded and illuminated, and the image accurately controlled to coincide with particular rotor azimuths. Liquid particles (primarily propylene glycol) were released into the flow downstream of the test section. This location was chosen to take advantage of the mixing action of the tunnel fan, and the distance before entering the test section, to establish a relatively uniform spatial distribution of particles in the flow approaching the rotor. Given the correct size and composition of the particles, and the right temperature and humidity of the air, the core of the vortex was comparatively void of particles. This provided a means of distinguishing the vortex from the surrounding flow in the rotor wake.

Table 3. Calibration matrix for VSB-54 balance

	J = 1	2	3	4	5	6
I = 1	0.00161	-0.01829	-1.1E-05	2.85E-05	0	1.23E-05
2	0.061664	0.061696	-4.1E-05	-5.8E-05	0	0.000141
3	-1.6E-05	3.36E-05	0.001629	-0.01849	0	-9.9E-06
4	1.64E-05	-1.6E-05	0.062126	0.062422	0	0.00037
5	0.000769	-1.6E-06	0.00071	0.001902	0	0.19434
6	0.000351	0.000373	0.00036	0.000386	0.1	2.96E-06

An argon laser beam was formed into two continuous, thin light sheets. Each light sheet was partially nulled and reflected off mirrors that directed them down onto the rotor wake. The mirrors were located 56 in. apart and were configured to rotate in the same plane. The plane defined by the light sheets could be rotated to any azimuth about an axis parallel to the rotor (when at zero shaft tilt), and could be translated in the streamwise direction. Either light sheet could be used to scan the flow for a feature of interest (in this case, the trailing vortex). Since the flow was unsteady, the image was "frozen" using an intensified, gated (about 0.0005 sec in this test) camera. By aiming the nulled region of each light sheet at the center of the vortex, the coordinates of the vortex segment in view could then be determined by triangulation.

A schematic of the setup for visualizing the flow is shown in figure 11. Elements of the light-sheet system appear in figure 12 above the model rotor. A detailed view of the two directable light sheets, along with embedded

reference lines that precisely locate the target, are shown in figure 13. This unique targeting system is referred to as LLS-ER (laser light-sheet system with embedded references).

Discussion of Results

Control Settings

Two methods were used for setting the angle of the rotor tip-path plane, α_{tp} . The first method involved setting the shaft tilt of the rotor stand to a given angle and then adjusting the cyclic pitch to eliminate blade flap. In the second method, the shaft tilt angle of the rotor stand was fixed at 0° and the cyclic pitch was adjusted to give the desired angle for the tip-path plane. Balance and blade pressure data were obtained for a range of rotor speeds and tip-path plane angles using both methods. The run numbers corresponding to these different conditions are given in tables 4 and 5.

Table 4. Run numbers for α_{tp} based on shaft tilt and zero blade flap

Tip-path plane, degrees	Rotor, RPM				
	1200	1500	1750	2000	2250
0.5	162	164	166	168	170
1	62	72	82	92	174
1.5	148	152	156	158	160
2	68	74	84	94	104
2.5	108	172	112	114	116
3	64	76	86	96	106
4	70	78	88	98	
5	66	80	90	100	

Table 5. Run numbers for α_{tp} based on blade flap and zero shaft tilt

Tip-path plane, degrees	Rotor, RPM				
	1200	1500	1750	2000	2250
0	118	130	138	176	
0.5	122	132	140	178	
1	124	134	142	184	
1.5	126	136	144	186	

The collective and cyclic pitch settings required in this test are shown in figure 14. Blade bending loads are presented in figure 15 for the case when the tip-path plane angle is obtained by tilting the shaft while maintaining zero blade flap. For $1^\circ \leq \alpha_{\text{tp}} \leq 5^\circ$, the steady component of the flap-bending moment increased slightly with RPM as well as with increases in the angle of the tip-path plane, but was always less than 25 in-lb in magnitude. The oscillatory component generally decreased with RPM from around 85 in-lb to 50 in-lb.

The chordwise locations of the strain gages forming the bridge for measuring lead-lag bending were incorrectly selected. As a consequence, the bridge was dominated by the centrifugal force induced moment and was therefore disregarded. However, the chord bending moment can be calculated from the load on the drag link gage, which indicates a steady increase with RPM from around 100 in-lb to 310 in-lb. The oscillatory components from both chord bending and drag link gages show a relatively flat response for $\text{RPM} \leq 2000$, followed by a 60% increase at the highest RPM. In general, the chord bending moment decreased with increases in the angle of the tip-path plane.

Likewise, blade-bending loads are presented in figure 16 for the case when the tip-path plane angle was obtained by means of blade flap while maintaining zero shaft tilt. In this case the steady component of the flap-bending moment generally decreased with increases in RPM as well as with decreases in the angle of the tip-path plane. The oscillatory component decreased with increases in the angle of the tip-path plane. The response to changes in RPM was somewhat flatter than in the shaft tilt case. The steady component of chordwise bending (calculated from the load on the drag link) shows a steady increase with increases in RPM. Although generally lower in magnitude when compared with the shaft tilt case, the steady component of chordwise bending shows little sensitivity to the angle of the tip-path plane in both the shaft tilt and cyclic pitch cases. The oscillatory component generally decreases with increases in the angle of the tip-path plane. Although lower in magnitude than in the shaft tilt case, the trend with changes in RPM is similar.

Balance Loads

Rotor balance loads are presented in figure 17 for tip-path plane angles obtained by tilting the shaft while maintaining zero blade flap. In all cases the thrust coefficient was held fixed at $C_T = 0.0054$ and $\mu = 0.164$. For $1^\circ \leq \alpha_{\text{tp}} \leq 5^\circ$, the axial force correctly increases with the square of rotor RPM. Although more erratic, the torque exhibits a similar dependence on RPM. The torque decreases with increases in α_{tp} because of the reduction

in blade drag (induced and profile) that accompanies the decrease in collective pitch (recall fig. 14). The side and normal forces are due to the integrated effects of induced and profile drag, which also contribute to the rotor pitch and roll moments. Balance loads are given in figure 18 for tip-path plane angles obtained by cyclic pitch with zero shaft tilt. For the limited number of cases considered, the trends are similar to those for shaft tilt, except that the moments are smaller and less erratic.

Blade Pressures

Among the blade pressure transducers listed in table 1, archived data (either an electronic file or a report figure) from two absolute pressures (1U and 2U) and two differential pressures (9D and 15D) were selected to compare with the present test data. All of the pressure data presented from the present test have been averaged over 14 rotor revolutions.

Even when the test parameters are duplicated, blade pressures may not match because of differences in the relative size of the model rotor to the wind tunnel jet. This was demonstrated with data taken from the DNW and CEPRA 19 facilities for the same test conditions of $\mu = 0.16$, $M_{\text{at}} = 0.77$ (or $M_b = 0.66$), and $C_T = 0.0054$ and using the same model rotor as in the present test. Both facilities are open jet, but they differ in shape and size. To match the blade pressure response that was obtained in the DNW for $\alpha_{\text{tp}} = 1^\circ$, conditions in the CEPRA 19 were found to require $\alpha_{\text{tp}} = 3.5^\circ$ (ref. 22). Although some differences are apparent (fig. 19), the pressure responses were considered sufficiently similar with regard to the resulting acoustic radiation.

Since earlier data sets for a given tip-path plane angle could have been obtained using either shaft tilt or cyclic pitch, both approaches were investigated and the signal from a differential pressure near the leading edge (15D) was used for comparison. The results for three tip-path plane angles ($\alpha_{\text{tp}} = 0.5^\circ$, 1.0° , and 1.5°) are presented in figure 20. Based on the similarity between the pressure responses, the two approaches were considered equivalent.

While holding $C_T = 0.0054$ and $\mu = 0.16$ constant, the pressure response at $r/R = 0.80$, $x/c = 0.03$ provides an indication of the sensitivity of blade pressure to variations in Mach number (fig. 21) and tip-path plane angle (fig. 22). With α_{tp} fixed at 1° (fig. 21), the primary consequence of reducing the Mach number (constant μ means that Ω and V_∞ are simultaneously reduced) is a slight decrease in the magnitude of the pressure peaks and an advance in the time of occurrence of these peaks (to lower values of ψ). With M_b fixed at 0.66 (fig. 22),

a decrease in the tip-path plane angle induces a similar reduction in the magnitude of the pressure peaks; however, there appears to be no shift in the time of occurrence of these peaks.

Pressure responses at several radial (fig. 23) and chord (fig. 24) locations, all of which are for $C_T = 0.0054$, $\mu = 0.16$, and $M_{th} = 0.66$, indicate what positions on the surface of the blade are most sensitive to changes in the aerodynamic environment of the rotor. The results in figure 23 show that all of the pressures near the leading edge have equally large responses and contain numerous distinctive features that reflect the different interactions occurring with the trailing vortices that are present in the rotor wake. In contrast to these leading-edge responses, figure 24 shows a decrease in the pressure variation toward the aft portion of the blade chord. Although the data in these two figures are from both differential and absolute pressure transducers, the distinguishing difference in their response to BVI is due primarily to their location on the blade.

The tip-path plane was assumed to be the only significant parameter requiring adjustment to account for differences between the present closed test section conditions and those for the DNW test. The pressure response for three values of α_{tip} are compared with DNW data obtained for the same values of C_T , μ , and M_{th} . The differential pressure (15D) results shown in figure 25 indicate that numerous features are exhibited by each of the α_{tip} curves that are similar to those found in the DNW data for $\alpha_{tip} = 1^\circ$. The shape, frequency, and amplitude of the perturbations in the pressure response on the advancing blade during $20^\circ < \psi < 130^\circ$ bear the greatest similarity to the DNW data; however, there are differences in both the absolute value and phase. Those differences appear to be insensitive to how the nondimensional groups are formed (that is, using a instead of V_∞ serves only to emphasize the advancing side response relative to the retreating side). The CEPRA data also differed in absolute value on the advancing blade from the DNW data (recall fig. 19), but appear to show good agreement in the phase angles of these events.

Dynamic responses in terms of gage pressure, measured by an absolute transducer (2U) at $x/c = 0.03$ and $r/R = 0.955$, are compared with DNW gage pressure data in figure 26 to illustrate the effects of modest changes in M_{at} and α_{tip} . In all cases, the pressure perturbations on the advancing blade are similar and indicate that small changes in these two parameters have little effect on the advancing blade pressure. Although the number of perturbations during this interval is the same as in the DNW data, the amplitude of the perturbations is less. Another difference is the higher magnitude of the

pressure in the *LoTuS* test; however, this is possibly due to a difference in air density between the two tests.

Rotor Wake

The fact that the rotor blade is always operating in its own wake is well illustrated in figure 27 by CAMRAD/JA (Comprehensive Analytical Model of Rotorcraft Aerodynamics and Dynamics/Johnson Associates) calculations of the tip-vortex trajectories. This particular wake geometry was calculated for $C_T = 0.0054$, $M_{at} = 0.77$, $\mu = 0.16$, and $\alpha_{tip} = 1^\circ$ at intervals of $\Delta\psi = 15^\circ$. Focusing on the principal source of high-speed BVI noise, the segment of vortex trajectory that is shed when the blade moves past an azimuth of $\psi = 135^\circ$ bears the greatest interest. Following this segment, marked with a square symbol in figure 28, as it moves downstream (primarily by freestream convection) shows that several classical types of interaction occur. Designating blade #1 as the source of the shed vortex to be tracked, the first classical interaction occurs at $\psi = 285^\circ$ as blade #2 moves past this vortex segment with a nearly perpendicular intersection. The second classical interaction occurs at $\psi = 435^\circ$ as blade #1 moves past its own vortex segment with an oblique intersection. The final classical interaction occurs at $\psi = 585^\circ$ as blade #2 moves past this vortex segment with a parallel intersection. This particular interaction is the most critical in terms of BVI noise.

Tracking of the vortex segment depends on proper seeding of the flow as well as correct illumination of the cross section of interest. Introducing the seed material directly upstream of the rotor (in the settling chamber about 85 ft ahead of the rotor in this test) resulted in a dramatic display of the flow pattern induced by a particular trailing vortex (fig. 29a). Concentrated seeding has the advantage of emphasizing the gross features of the flow so that the location of the vortex can be readily identified. The disadvantage of concentrated seeding is that the particular features that are emphasized in the rotor wake are biased by the exact cross-stream position where the particles are introduced. A more uniform distribution of seed particles in the test section is achieved when the particles are released into the flow downstream of the rotor. This location allows more time for diffusion into the flow and also takes advantage of the mixing action of the tunnel fan. Increasing the proportion of particles released downstream, relative to those released directly upstream, lowers the biasing of the flow visualization and enables other features that might be present to be identified (fig. 29b). In this case there happens to be three vortices that are present in the flow. Vortex #2 was the only apparent vortex in figure 29a, whereas vortex #1 was the segment actually being tracked since its release at

$\psi = 135^\circ$. The most uniform distribution of seed particles in the test section is obtained when they are injected into the flow only at the downstream location (fig. 29c). The advantage offered by this condition is that real-time optical tracking of the vortex can be employed whenever meander is a problem. The disadvantage is that the population of seed particles reaching the test section may also be uniformly too small. In this case fewer particles will centrifuge away from the vortex core and the vortex will be less distinguishable from the remainder of the flow around it. This distinguishable change in the particle count is generally interpreted to be a reasonable estimate for the size of the vortex core.

To correctly map the spatial history of a given vortex segment requires tagging the small domain of fluid comprising that segment and following its subsequent excursion as part of the rotor wake. An equivalent experimental procedure would require briefly marking the fluid within the core of the vortex at the moment it is shed from the blade. Rather than marking the fluid and tracking the trajectory of the same segment of fluid as it moves through the wake, a hybrid approach was taken. The calculated streamwise location of the vortex segment for a given blade azimuth was used to determine the streamwise position of the plane of the light sheets. The reference line contained in each of the light sheets was then used to locate the position of the vortex within that plane (fig. 30). For example, if the plane of the light sheets was oriented perpendicular to the freestream direction, then aiming the light sheets at the center of the vortex would yield the crossflow location. Because of the flexibility in the present system for positioning the plane of the light sheets relative to the flow, several parameters must be known in order to determine the spatial location of the targeted region. These parameters are (1) the streamwise location of the light-sheet pivot, (2) the angle of the light-sheet plane relative to the flow, and (3) the angles defining the direction of each light sheet.

The measured trajectories of vortex segments shed at $\psi = 112^\circ$ and $\psi = 135^\circ$ are shown in figure 31. The results show both segments moving inboard and initially rising above the rotor disk as they are convected downstream. Included in the top view are small figures indicating the azimuthal age of the vortex segment, since being shed by the rotor blade. The segment associated with $\psi = 112^\circ$ was tracked for a greater distance and appears to be drawn downward over the aft portion of the rotor disk. The calculated trajectories using CAMRAD/JA for vortex segments shed when $\psi = 105^\circ$, $\psi = 120^\circ$, and $\psi = 135^\circ$ show the same trends as the measured results, although the magnitudes of the crossflow and vertical movements are different.

Conclusions

Blade surface pressure depends on the angle of the tip-path plane, but appears to be independent of whether this angle is obtained using shaft tilt or cyclic pitch. Surface pressures near the leading edge appear to be equally sensitive along the entire outer half of the blade, but exhibit a marked decrease in sensitivity as the distance along the chord increases.

The shape and number of pressure perturbations caused by blade-vortex interactions on the advancing blade are similar to those obtained in an earlier DNW test. However, the amplitude and phase of the perturbations were slightly different for the range of tip-path plane angles in this study.

Downstream injection of seed particles yields the most uniform seeding distribution in the test section. Comparatively close upstream injection of seed particles reveals selected gross features of the flow and is dependent on the lateral (or cross-stream) location of the injection point.

The diameter of the core region of the trailing vortex is approximately equal to the thickness of the blade at the tip. The laser light-sheet system with embedded references proved to be an accurate and simple means for ascertaining the spatial coordinates of the trailing vortex.

The measured trajectories of vortex segments shed from the rotor blade at particular azimuths on the advancing side show an inboard movement toward the rotor hub and an arched vertical movement that is positive in the second quadrant and negative in the first quadrant. These trends were found to be in agreement with CAMRAD/JA calculations, but the magnitudes were slightly different.

References

1. Sakowsky, P. C.; and Charles, B. D.: Noise Measurement Test Results for AH-1G Operational Loads Survey. Vols. I and II, Bell Helicopter Co. Report 299-099-831, 1976.
2. Boxwell, D. A.; and Schmitz, F. H.: Full-Scale Measurements of Blade-Vortex Interaction Noise. Presented at the 36th Annual National Forum of the American Helicopter Society, Washington, DC, 1980.
3. Boxwell, D. A.; Schmitz, F. H.; Spletstoeser, W. R.; and Schultz, K. J.: Model Helicopter Rotor High-Speed Impulsive Noise: Measured Acoustics and Blade Pressures. Presented at the 9th European Rotorcraft Forum, Paper No.17, Stresa, Italy, 1983.

4. Dadone, L. U.; Caradonna, F. X.; Ramachandra, K.; Silva, M. J.; and Poling, D.: The Prediction of Loads on the Boeing Helicopters Model 360 Rotor. Presented at the 45th Annual National Forum of the American Helicopter Society, Boston, MA, May 1989.
5. Lorber, P. F.: Aerodynamic Results of a Pressure-Instrumented Model Rotor Test at the DNW. Presented at the 46th Annual National Forum of the American Helicopter Society, Washington, DC, 1990.
6. Schmitz, F. H.; Boxwell, D. A.; Lewy, S.; and Dahan, C.: A Note on the General Scaling of Helicopter Blade-Vortex Interaction Noise. Presented at 38th Annual National Forum of the American Helicopter Society, Anaheim, CA, 1982.
7. Boxwell, D. A.; Schmitz, F. H.; Splettstoesser, W. R.; and Schultz, K. J.: Helicopter Model Rotor Blade Vortex Interaction Impulsive Noise: Scalability and Parametric Variations. *Journal of the American Helicopter Society*, vol. 32, no. 1, 1987.
8. Yu, Y. H.; Tung, C.; Gallman, J.; Splettstoesser, W. R.; Schultz, K. J.; Spiegel, P.; Rahier, G.; and Michea, B.: Aerodynamics and Acoustics of Rotor Blade-Vortex Interactions: Analysis Capability and its Validation. Paper AIAA 93-4332, presented at 15th AIAA Aeroacoustics Conference, Long Beach, CA, 1993.
9. Beaumier, P.; Prieur, J.; Rahier, G.; Demargne, A.; Tung, C.; Gallman, J. M.; Yu, Y. H.; Kube, R.; Van der Wall, B. G.; Schultz, K. J.; Splettstoesser, W. R.; Brooks, T. F.; Burley, C. L.; and Boyd, D. D.: Effect of Higher Harmonic Control on Helicopter Rotor Blade-Vortex Interaction Noise and Initial Validation. AGARD Meeting, Berlin, Germany, 1994.
10. Tangler, J. L.: Schlieren and Noise Studies of Rotors in Forward Flight. *Proceedings of 33rd Annual Forum of the American Helicopter Society*, Washington, DC, 1977.
11. Parthasarathy, S. P.; Cheo, Y. I.; and Back, L. H.: Wide-Field Shadowgraph Flow Visualization of Tip Vortices Generated by a Helicopter Rotor. *AIAA 18th Fluid Dynamics and Plasmadynamics and Laser Conference*, AIAA 85-1557, Cincinnati, OH, 1985.
12. Norman, T. R.; and Light, J. S.: Rotor Tip Vortex Geometry Measurements Using the Wide-Field Shadowgraph Technique. *Journal of the American Helicopter Society*, vol. 32, no. 2, 1987, pp. 40-50.
13. Bagai, A.; Leishman, J. G.; and Samak, D. K.: A Study of Rotor Wake Development and Wake/Body Interaction in Hover. *Proceedings of the American Helicopter Society International Specialists' Meeting on Rotorcraft Basic Research*, Georgia Institute of Technology, Atlanta, GA, 1991.
14. Light, J. S.; Frerking, A. A.; and Norman, T. R.: Application of the wide-Field Shadowgraph Technique to Helicopters in Forward Flight. *Proceedings of the 46th Annual Forum of the American Helicopter Society*, Washington, DC, 1990.
15. Leishman, J. G.; and Bagai, A.: Fundamental Studies of Rotor Wakes in Low Speed Forward Flight Using Wide-Field Shadowgraphy. *AIAA 9th Applied Aerodynamics Conference*, AIAA 91-3232, Baltimore, MD, 1991.
16. Brand, A. G.; Komerath, N. M.; and McMahon, H. M.: Results from Laser Sheet Visualization of a Periodical Rotor Wake. *AIAA 26th Annual Science Meeting*, AIAA 88-0192, Reno, NV, 1988.
17. Leighty, B. D.; Rhodes, D. B.; Franke, J. M.; and Jones, S. B.: A Synchronous Strobed laser Light Sheet for Rotor Flow Visualization. *NASA TM-4266*, 1991.
18. Elliott, J. W.; Peryea, M. A.; Brand, A. G.; and Wood, T. L.: Induced Inflow Velocity and Blade Surface Pressure Measurements for a Helicopter Model in Forward Flight. *NASA TM-104224*, 1992.
19. Ghee, T. A.; and Elliott, J. W.: The Wake of a Small-Scale Rotor in Forward Flight using Flow Visualization. *Journal of the American Helicopter Society*, vol. 40, no. 3, 1995, pp. 52-65.
20. Yu, Y. H.; Gmelin, B.; Heller, H.; Philippe, J. J.; Mercker, E.; and Preisser, J. S.: HHC Aeroacoustics Rotor Test at the DNW—The Joint German/French/U.S. HART Project. *Proceedings of the 20th European Rotorcraft Forum*, Amsterdam, Netherlands, 1994.
21. Splettstoesser, W. R.; Schultz, K. J.; Boxwell, D. B.; and Schmitz, F. H.: Helicopter Model Rotor-Blade Vortex Interaction Impulsive Noise: Scalability and Parametric Variations. *NASA TM-86007*, 1984.
22. Boxwell, D. A.; Schmitz, F. H.; Splettstoesser, W. R.; Schultz, K. J.; Lewy, S.; and Caplot, M.: A Comparison of the Acoustic and Aerodynamic Measurements of a Model Rotor Tested in Two Anechoic Wind Tunnels. *NASA TM-88364*, 1986.

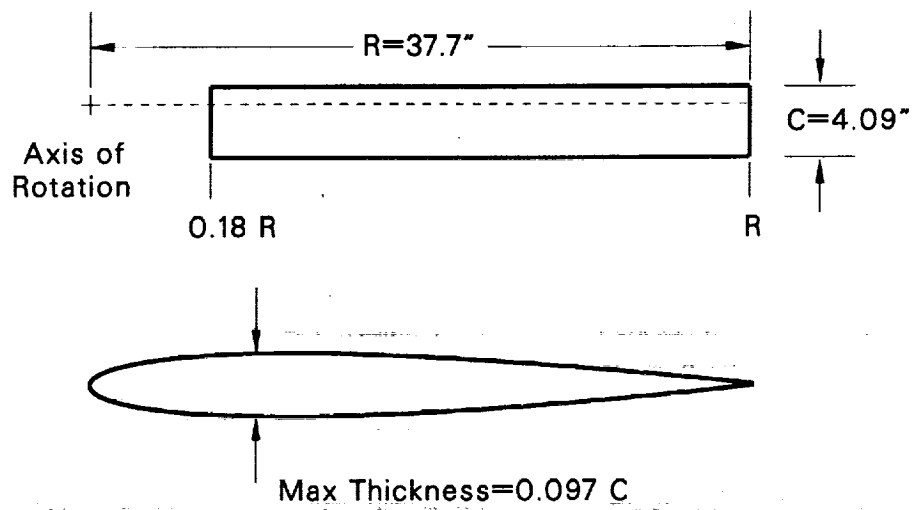


Figure 1. Dimensions of model OLS rotor blade (modified BHT 540).

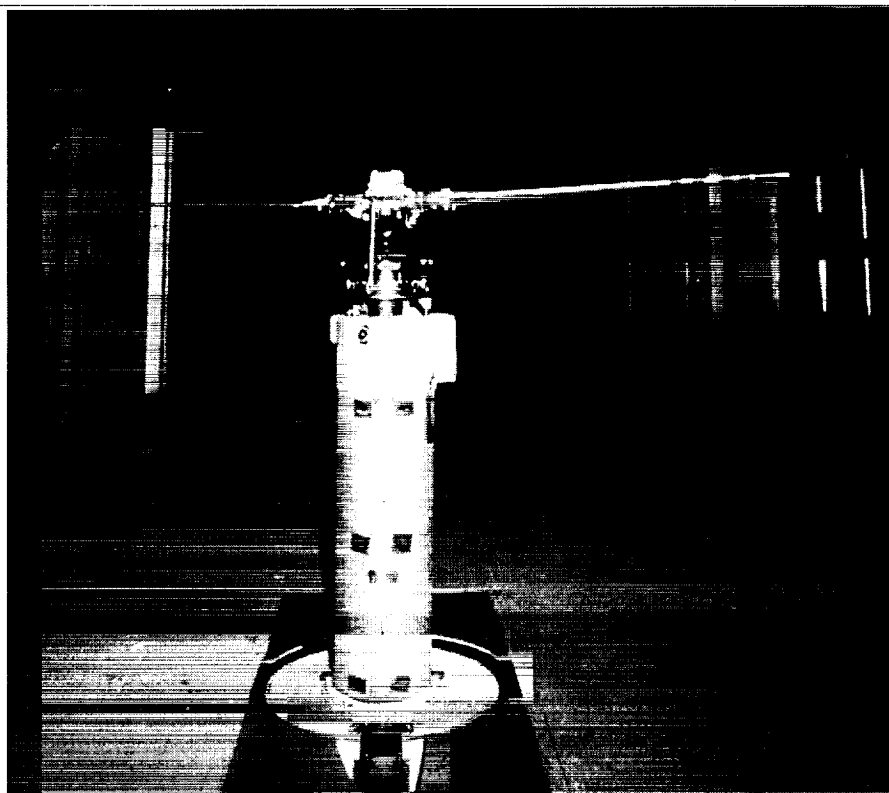


Figure 2. Installation of model rotor in 7- by 10-Foot Wind Tunnel.

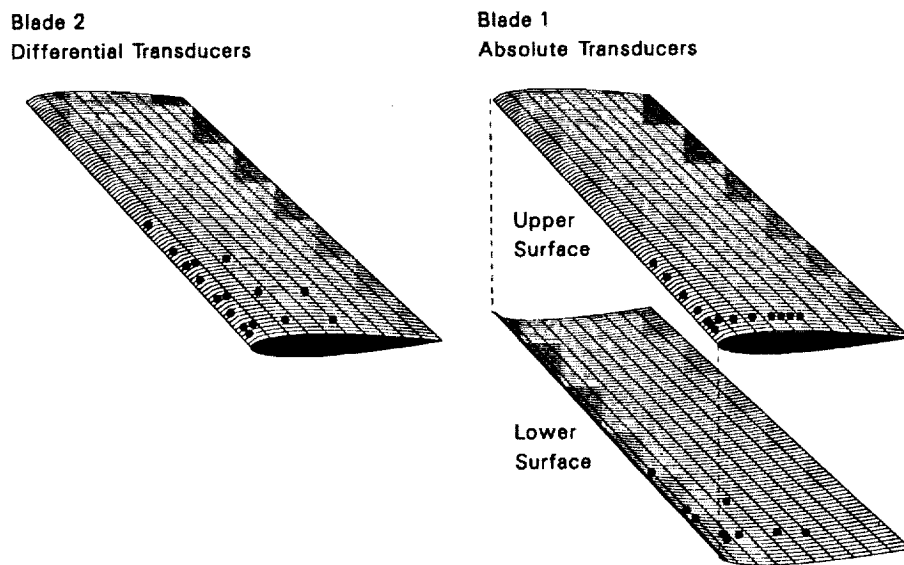


Figure 3. Location of absolute and differential pressure transducers.

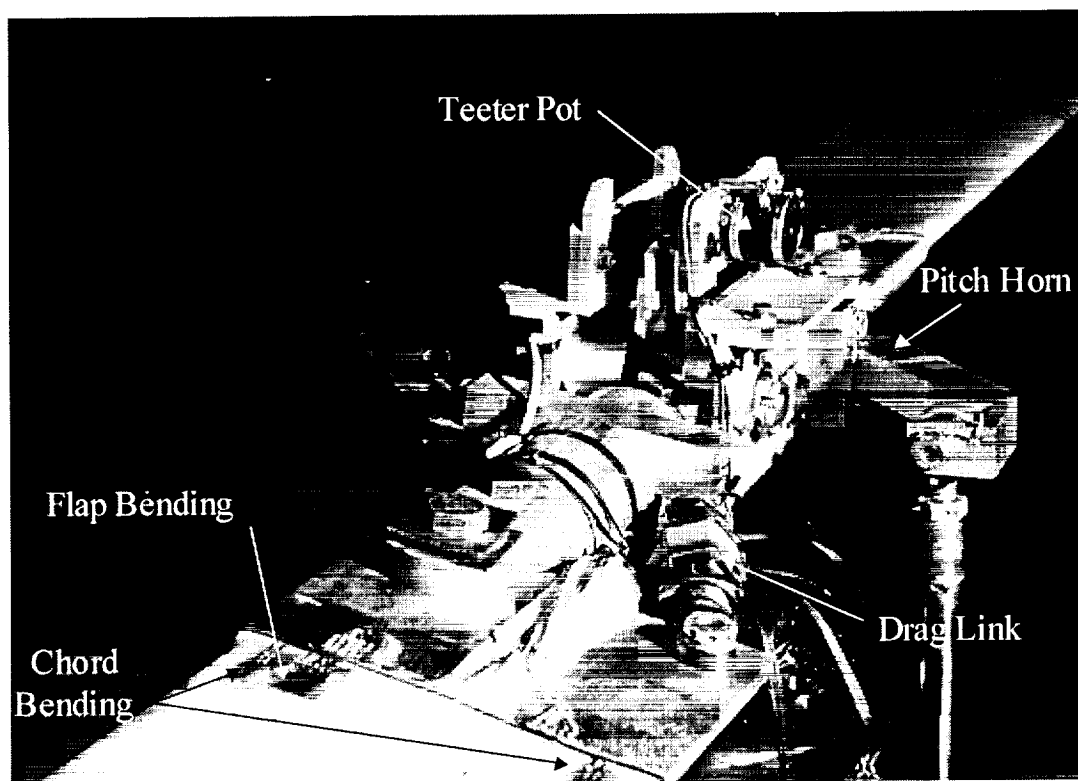


Figure 4. Rotor safety-of-flight gages.

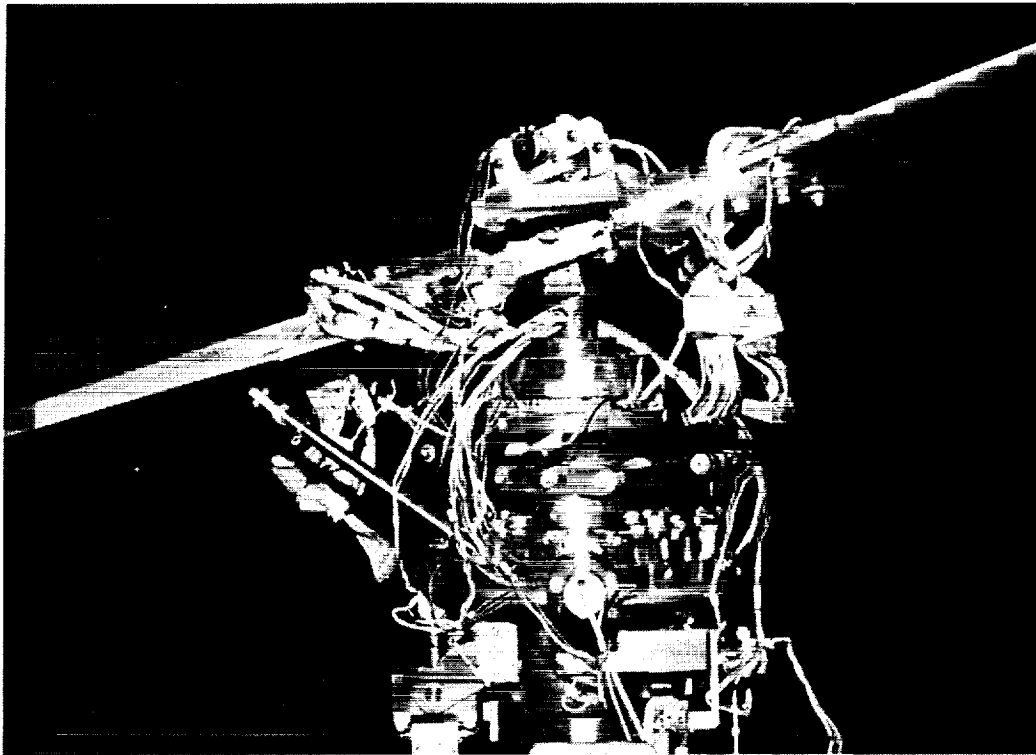


Figure 5. Excitation and signal wires from safety gages and pressure transducers.

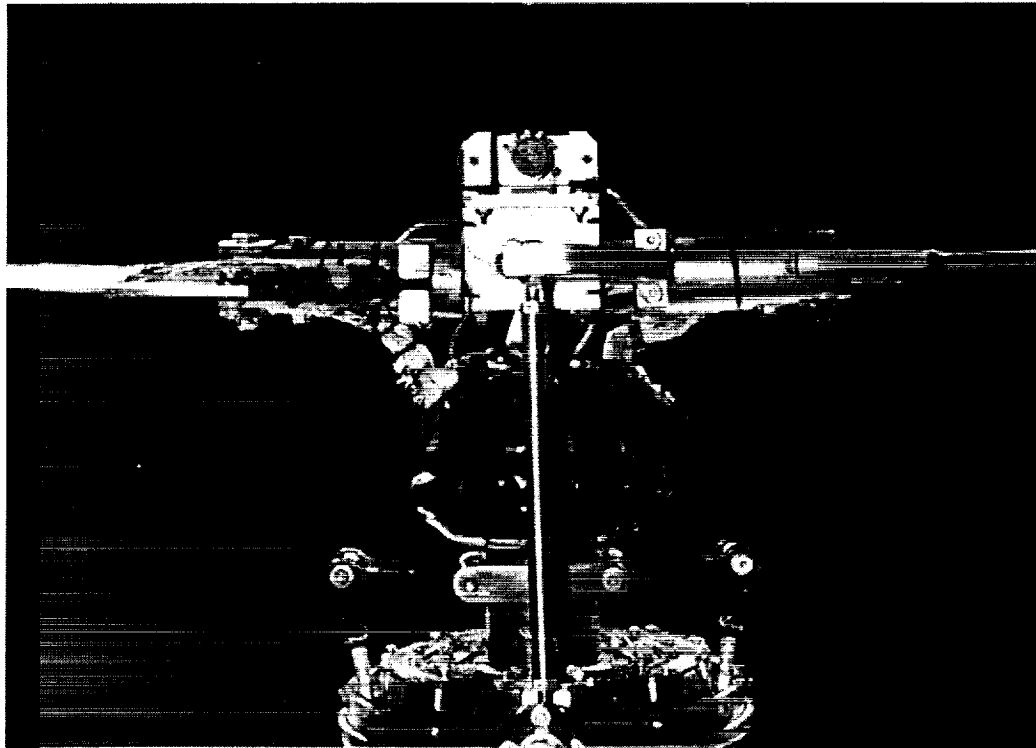


Figure 6. Instrumentation wires secured with tape and string.

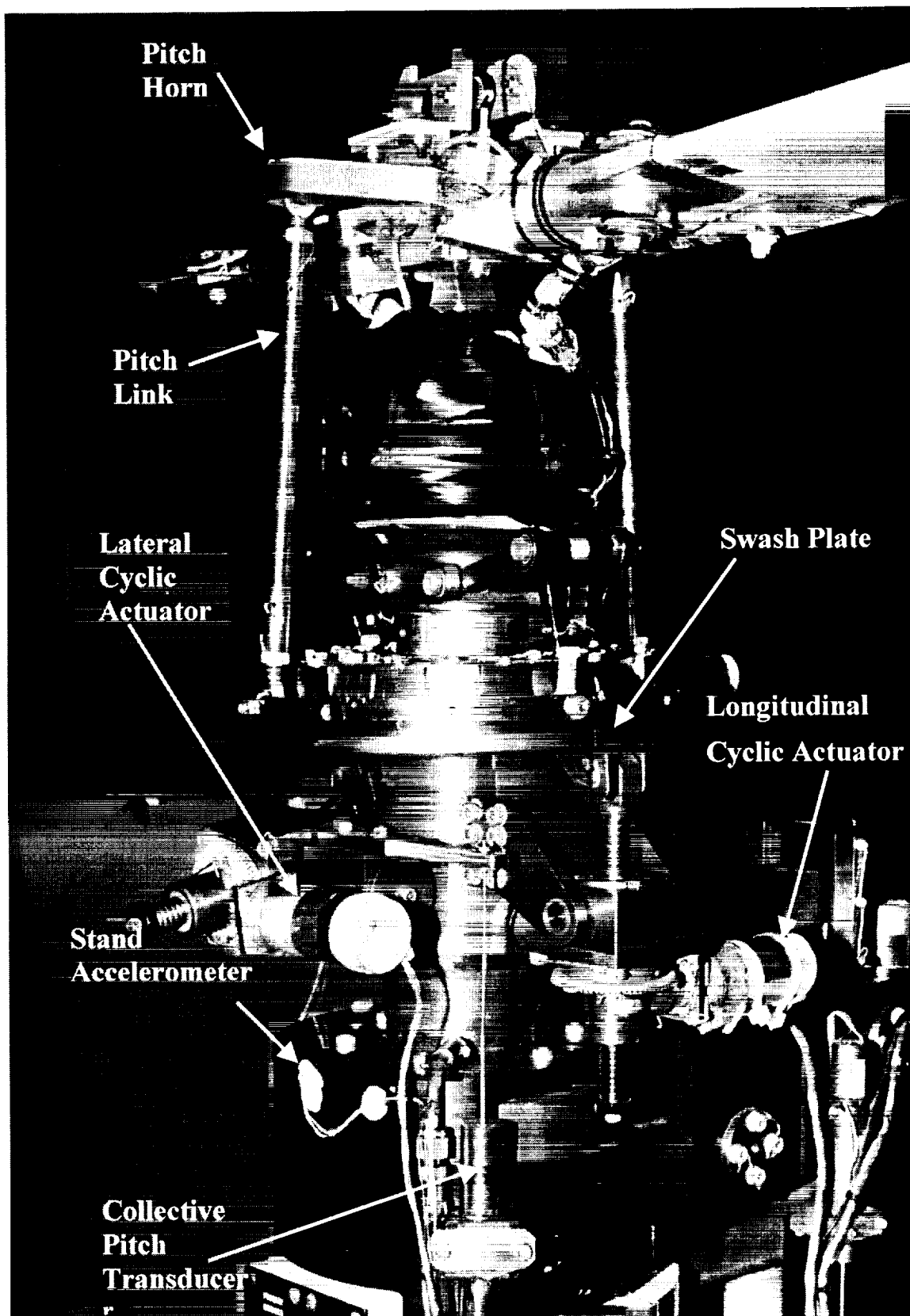


Figure 7. Blade pitch controls.

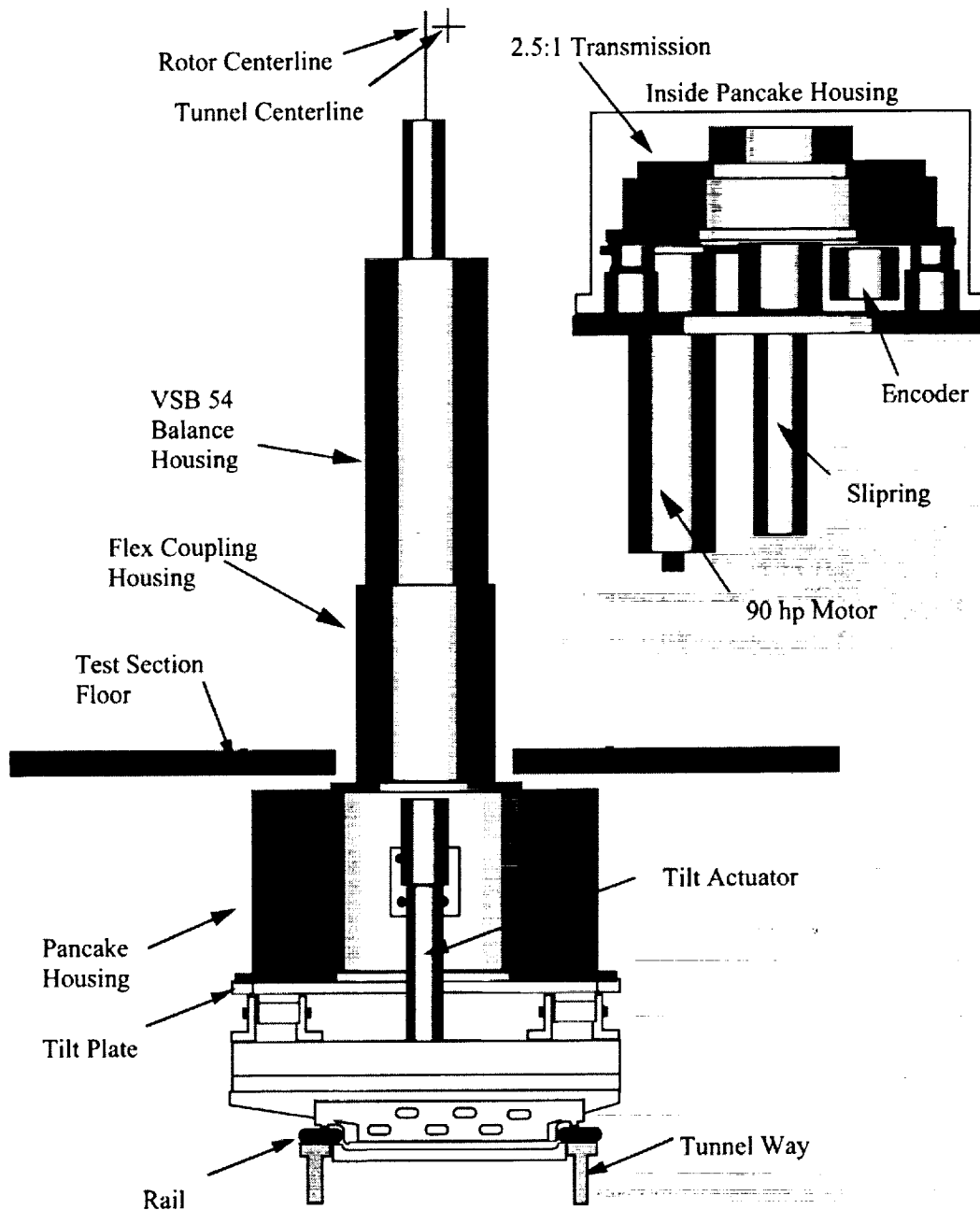


Figure 8. Front view of rotor stand installation in 7- by 10-Foot Wind Tunnel.

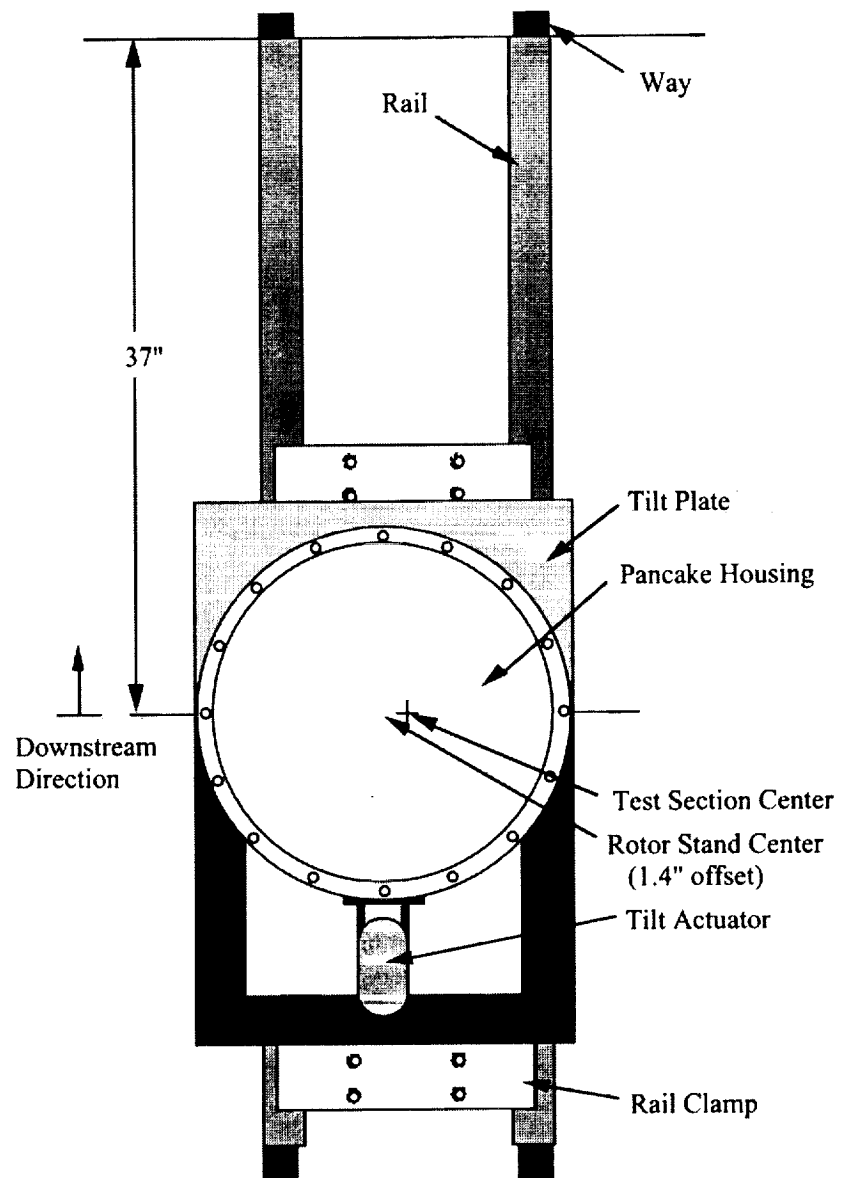


Figure 9. Top view of rotor stand installation in 7- by 10-Foot Wind Tunnel.

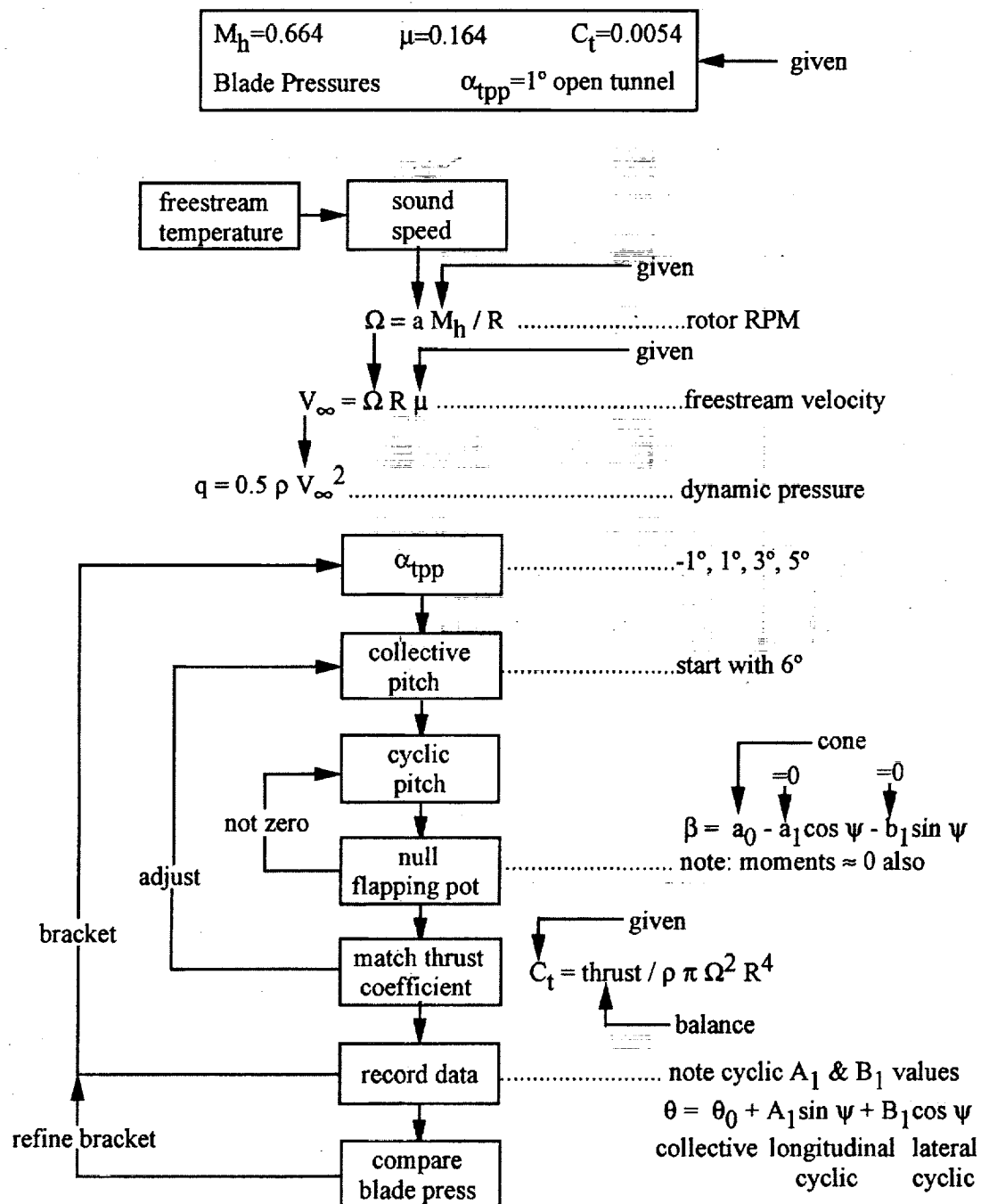


Figure 10. Procedure for matching DNW test conditions.

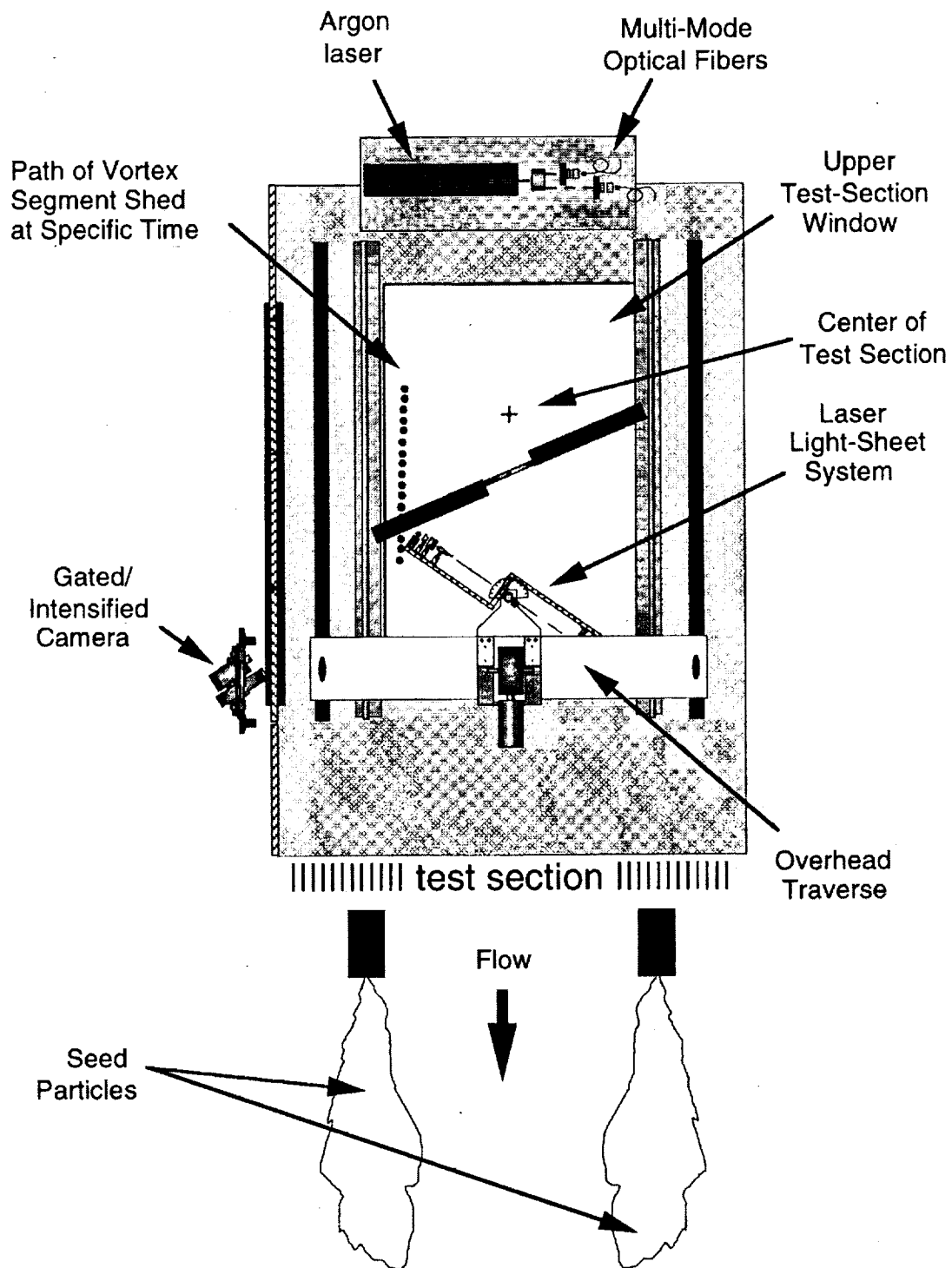


Figure 11. Setup for flow visualization.

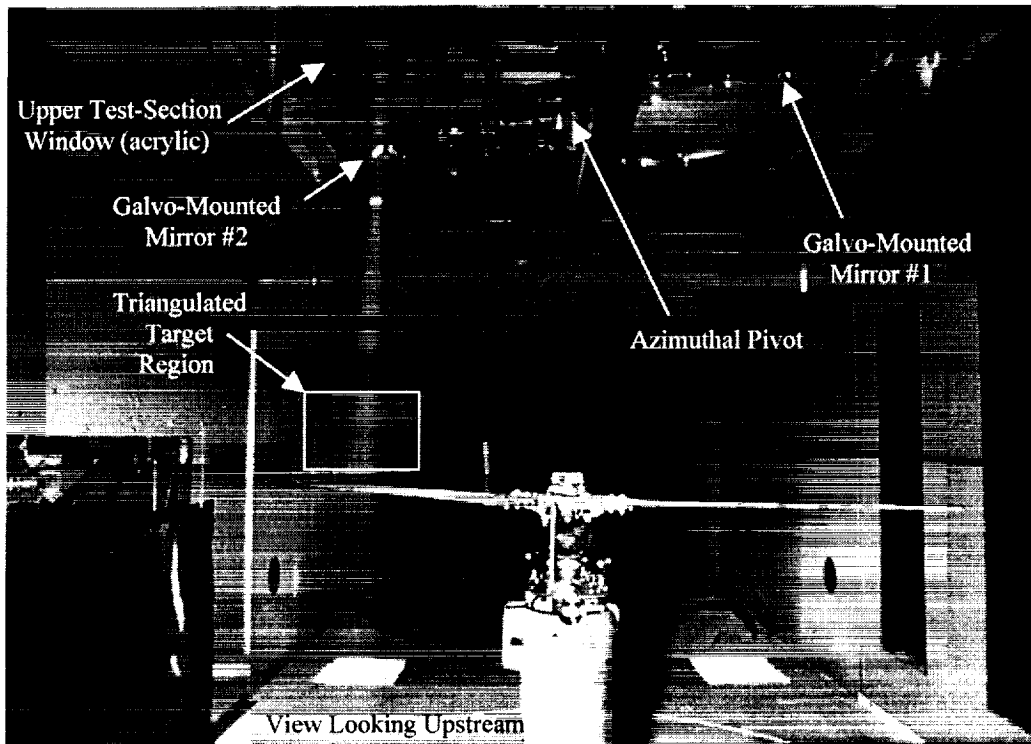


Figure 12. Elements of the light-sheet system.

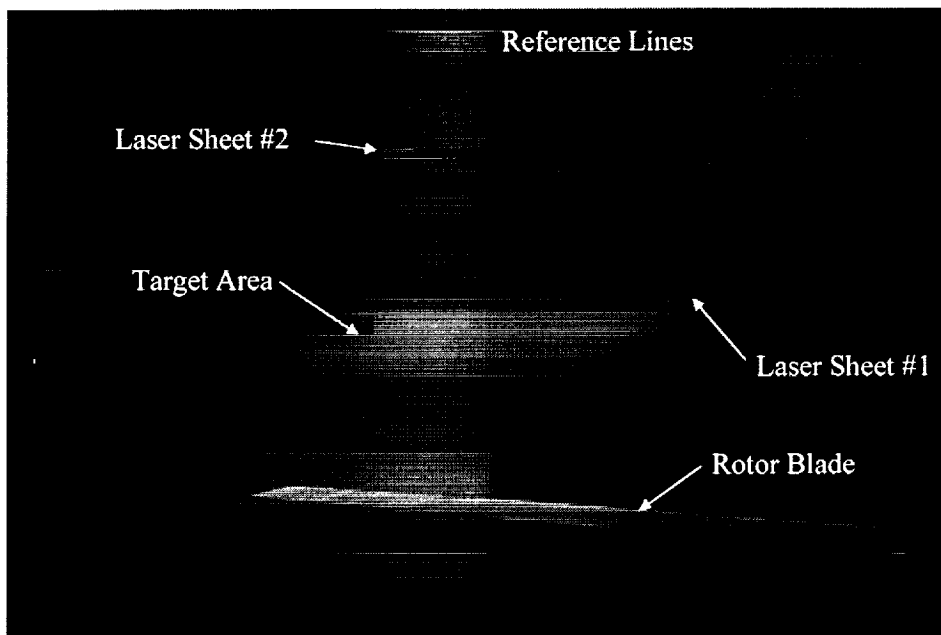


Figure 13. Detailed view of directable light sheets with coincident reference lines.

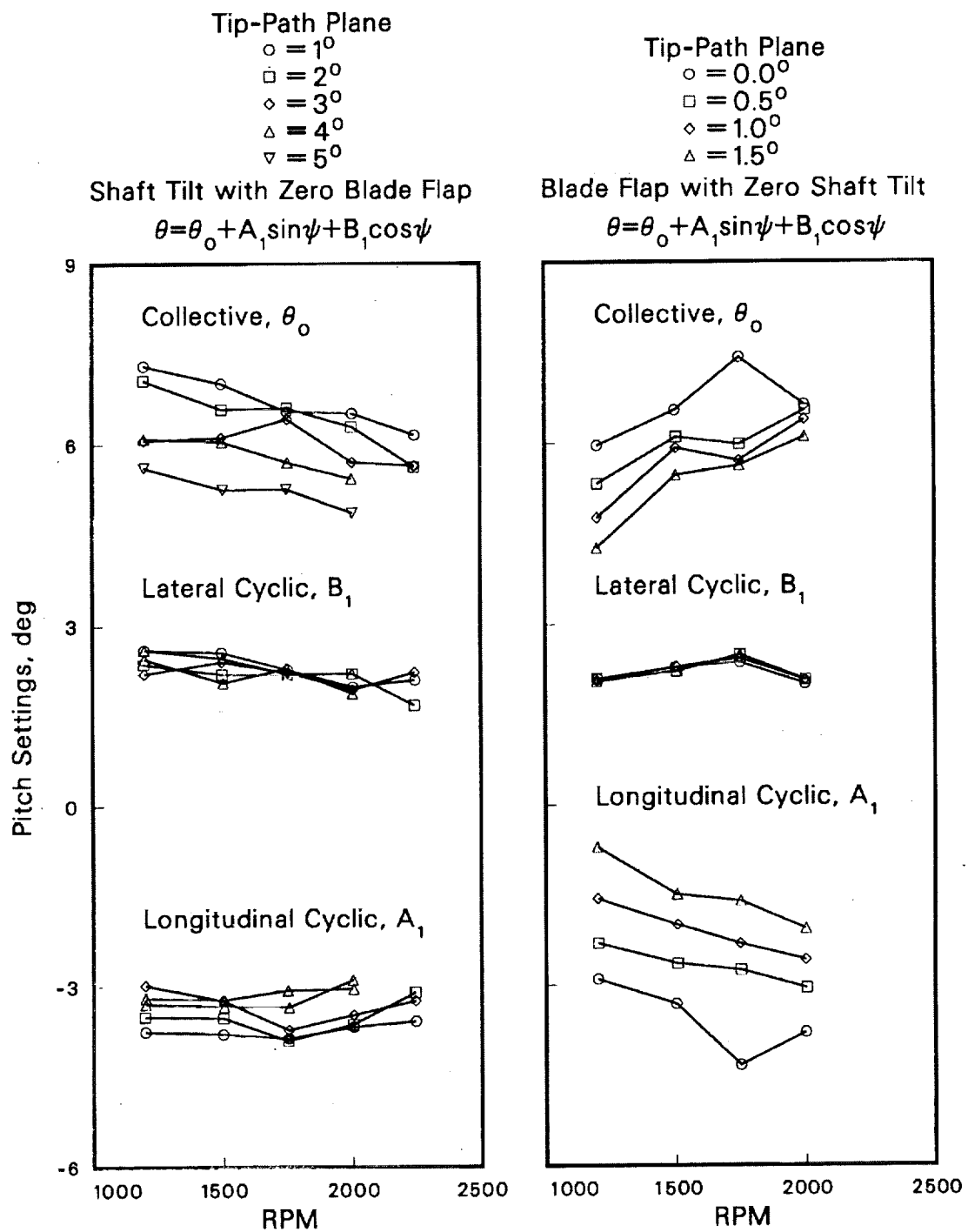


Figure 14. Rotor-blade pitch settings required for various tip-path plane angles ($C_T=0.0054$, $\mu=0.164$, M_h and M_{at} varying).

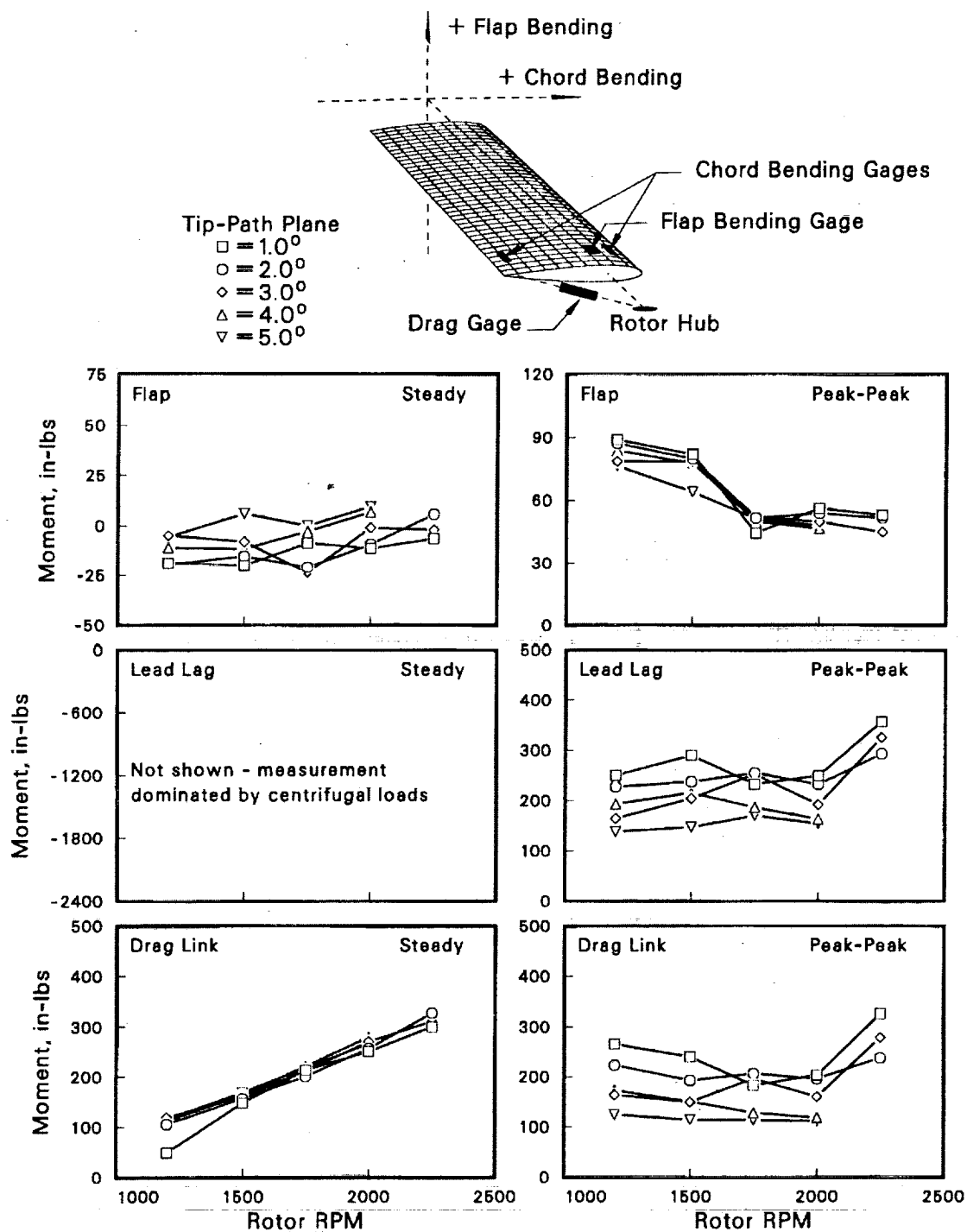


Figure 15. Bending loads for various α_{tpp} obtained by shaft tilt with zero blade flap.

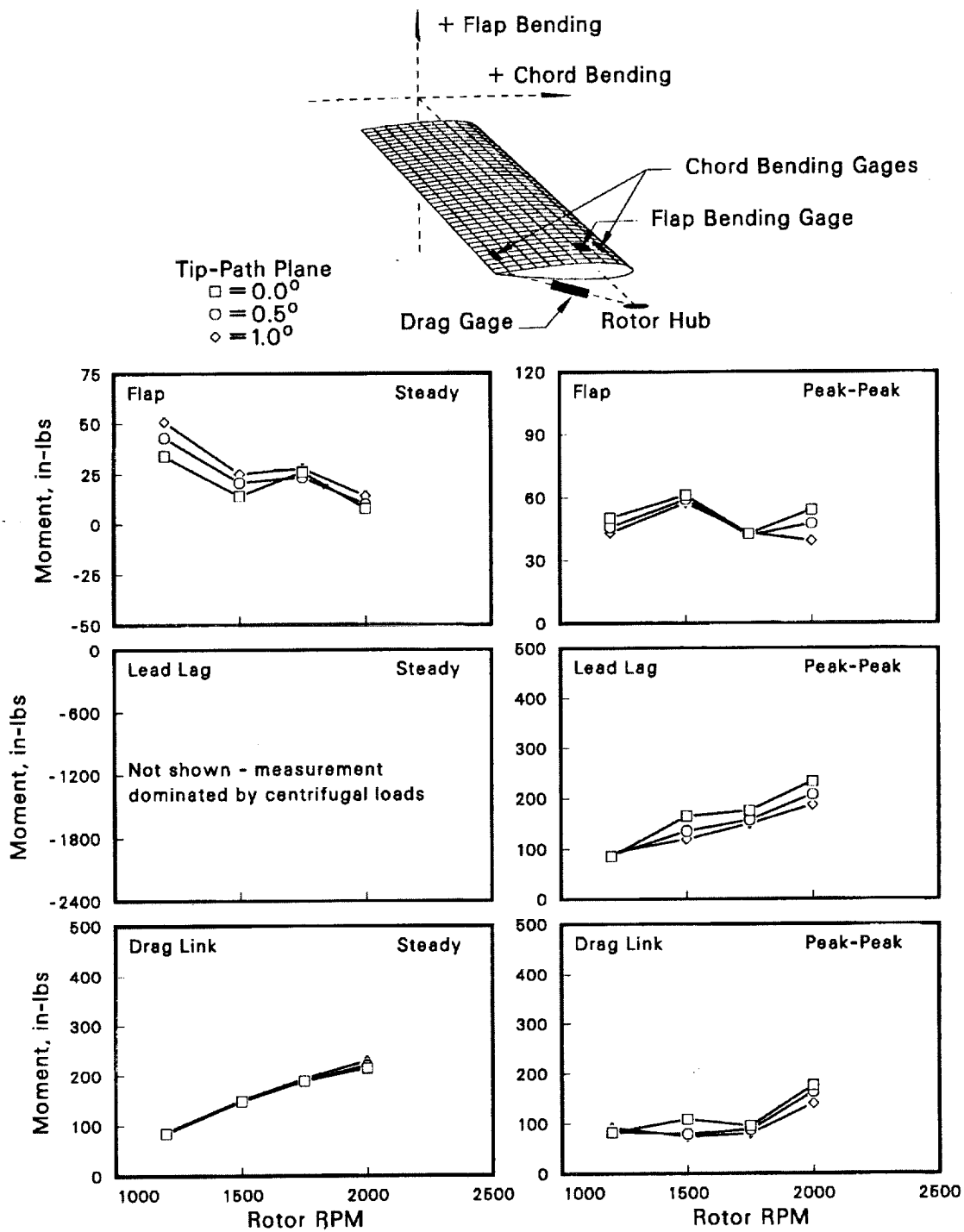


Figure 16. Bending loads for various α_{tp} obtained by cyclic pitch with zero shaft tilt.

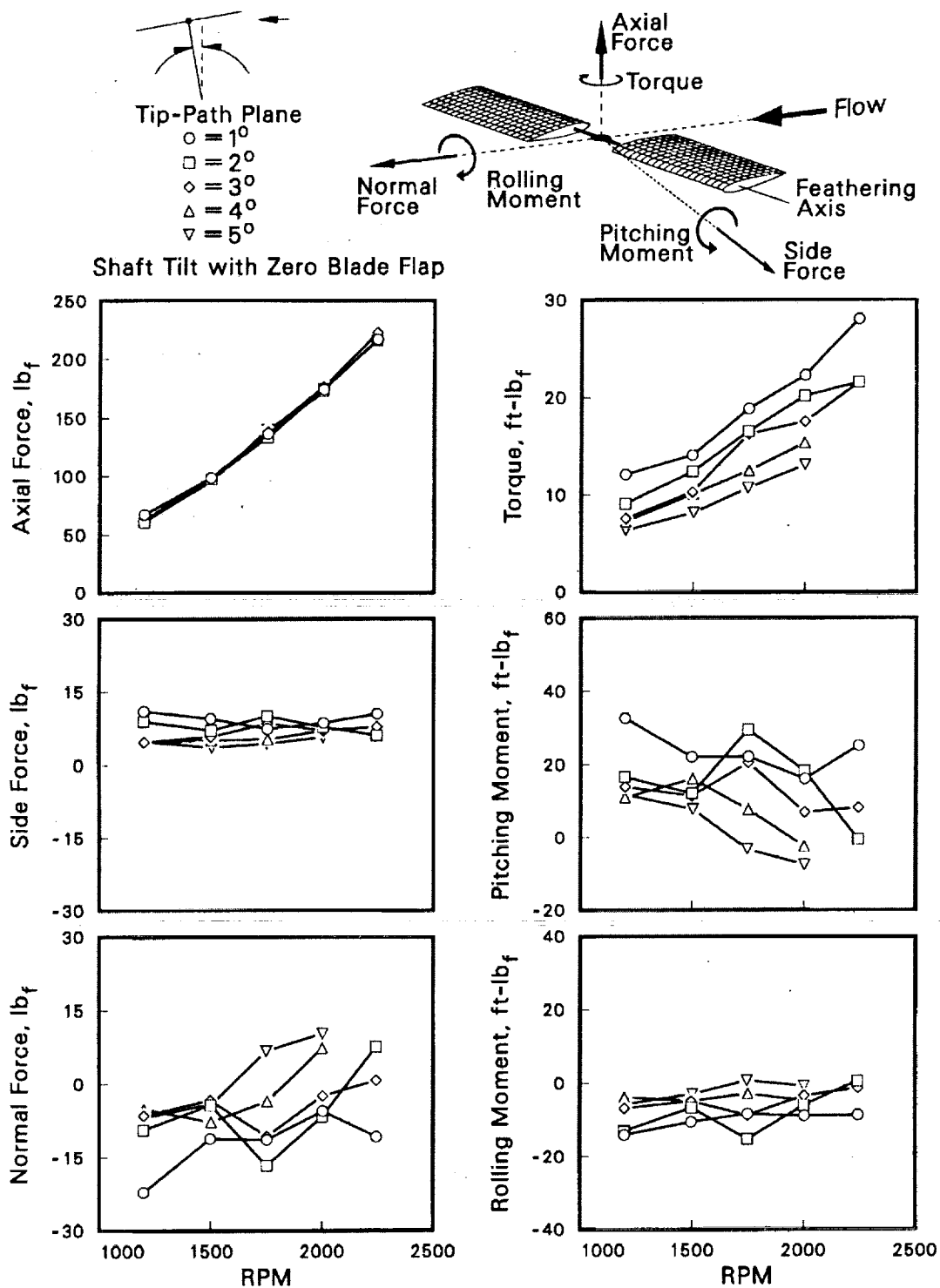


Figure 17. Balance loads for various α_{tpp} obtained by shaft tilt with zero blade flap.

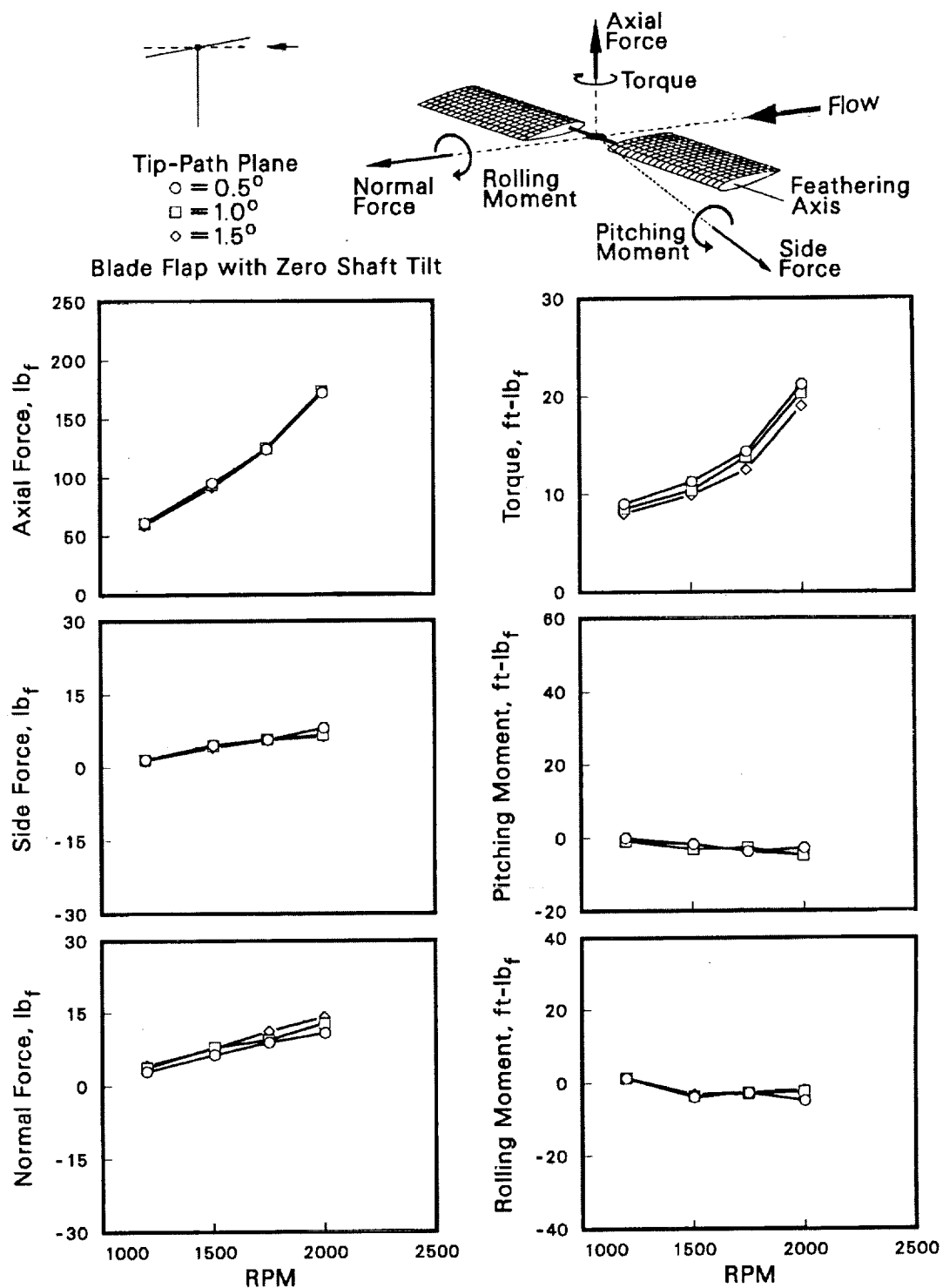


Figure 18. Balance loads for various α_{tp} obtained by cyclic pitch with zero shaft tilt.

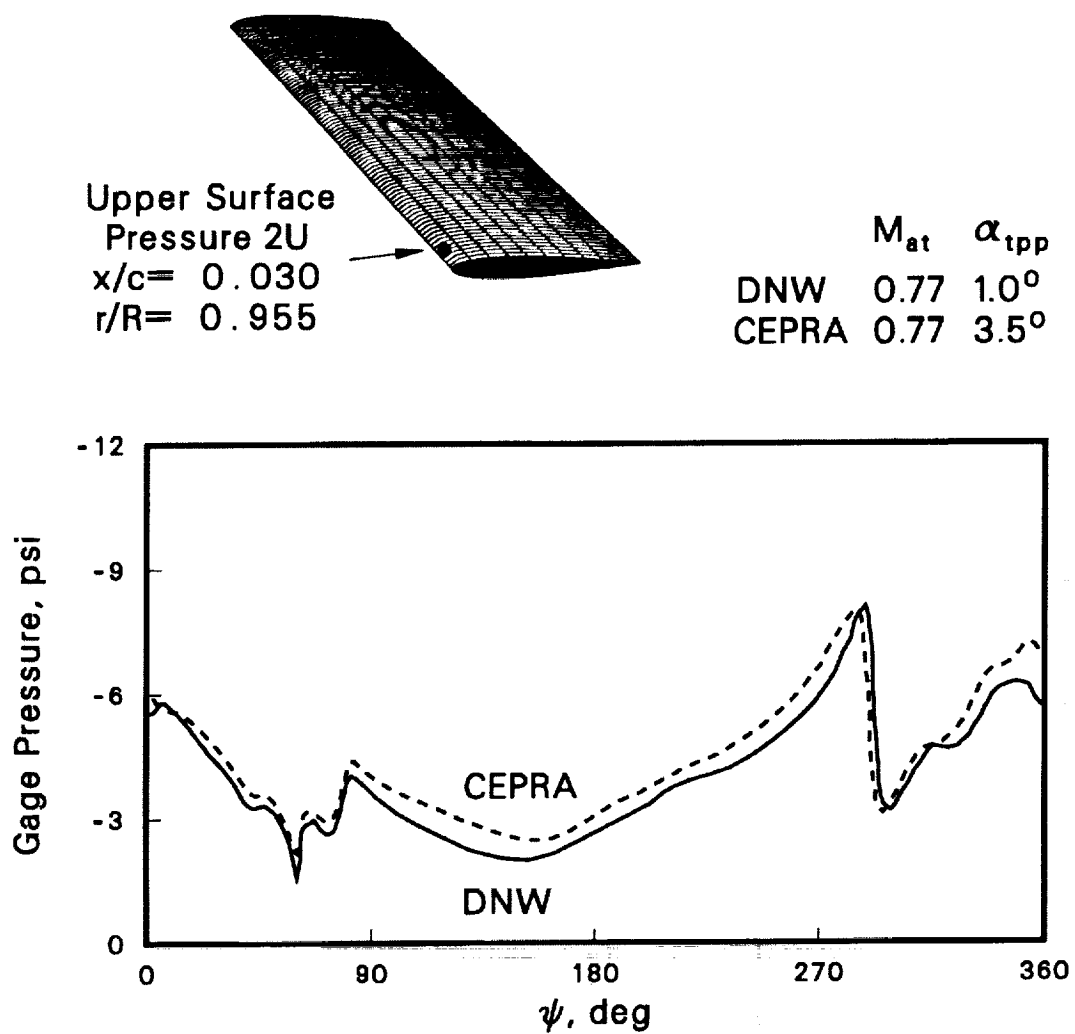


Figure 19. Blade pressures from tests in CEPRA-19 and DNW facilities (ref. 22).

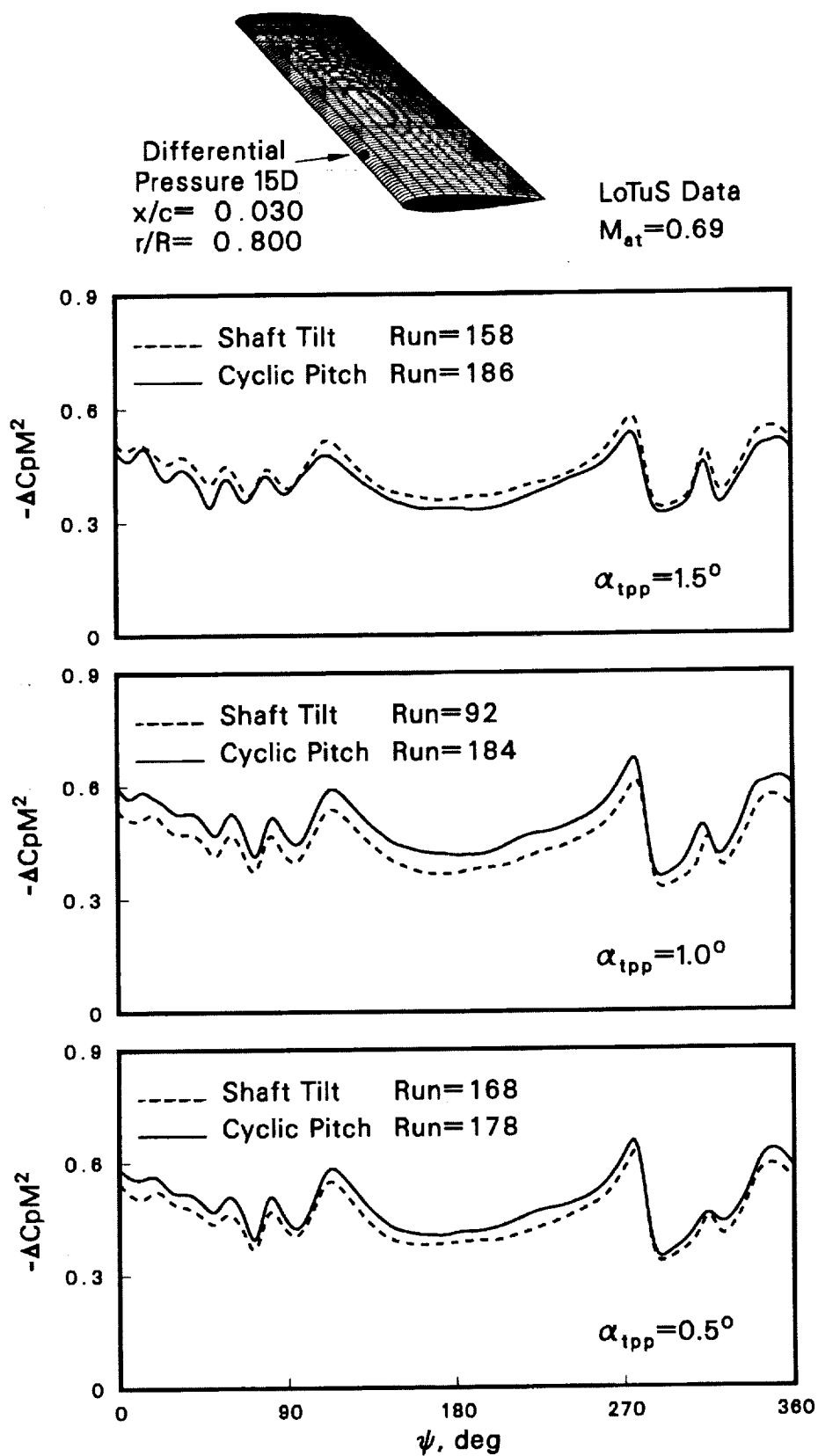


Figure 20. Blade pressure using two methods for obtaining the same tip-path plane.

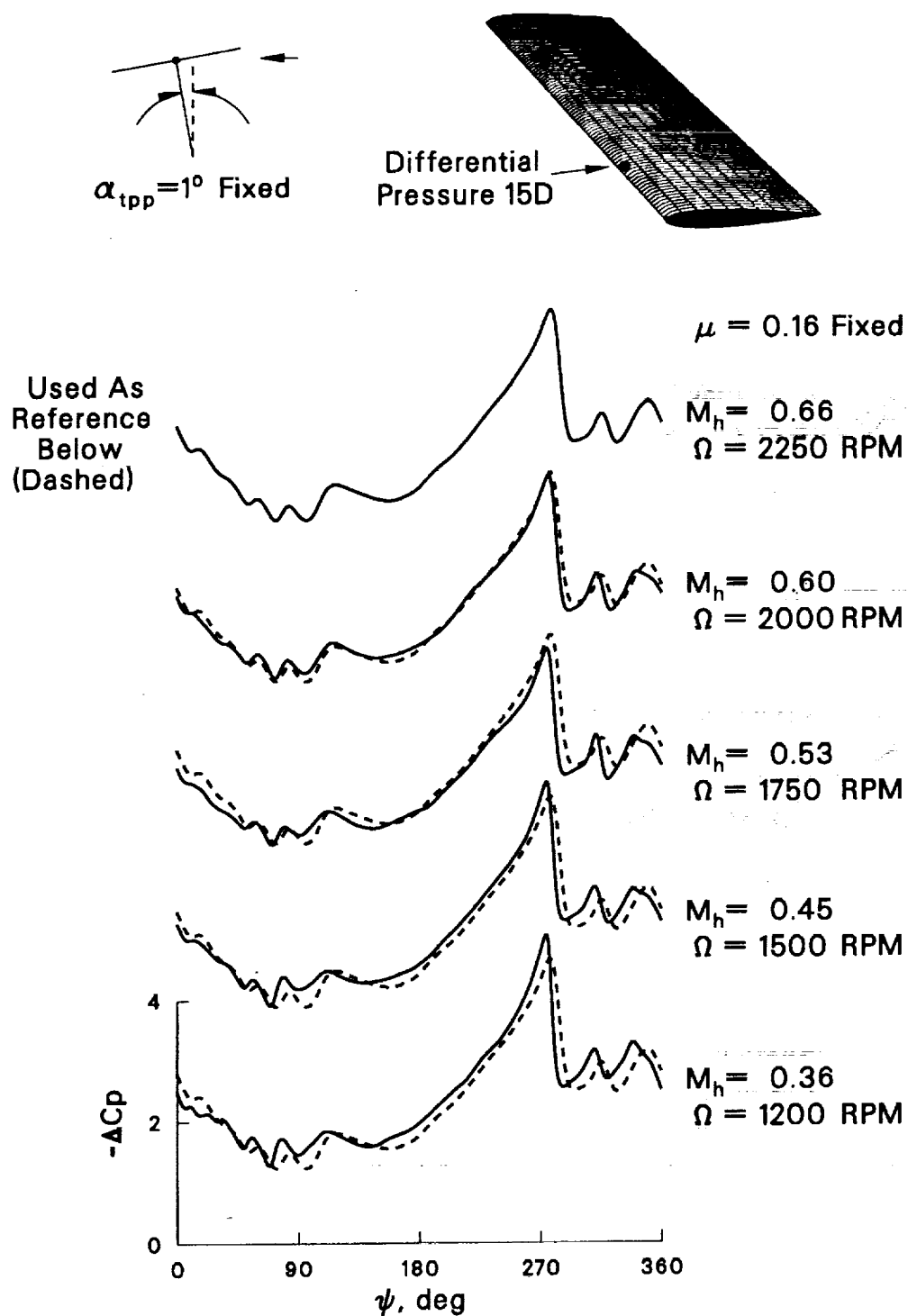


Figure 21. Periodic pressure response for range of Mach numbers (α_{tp} fixed).

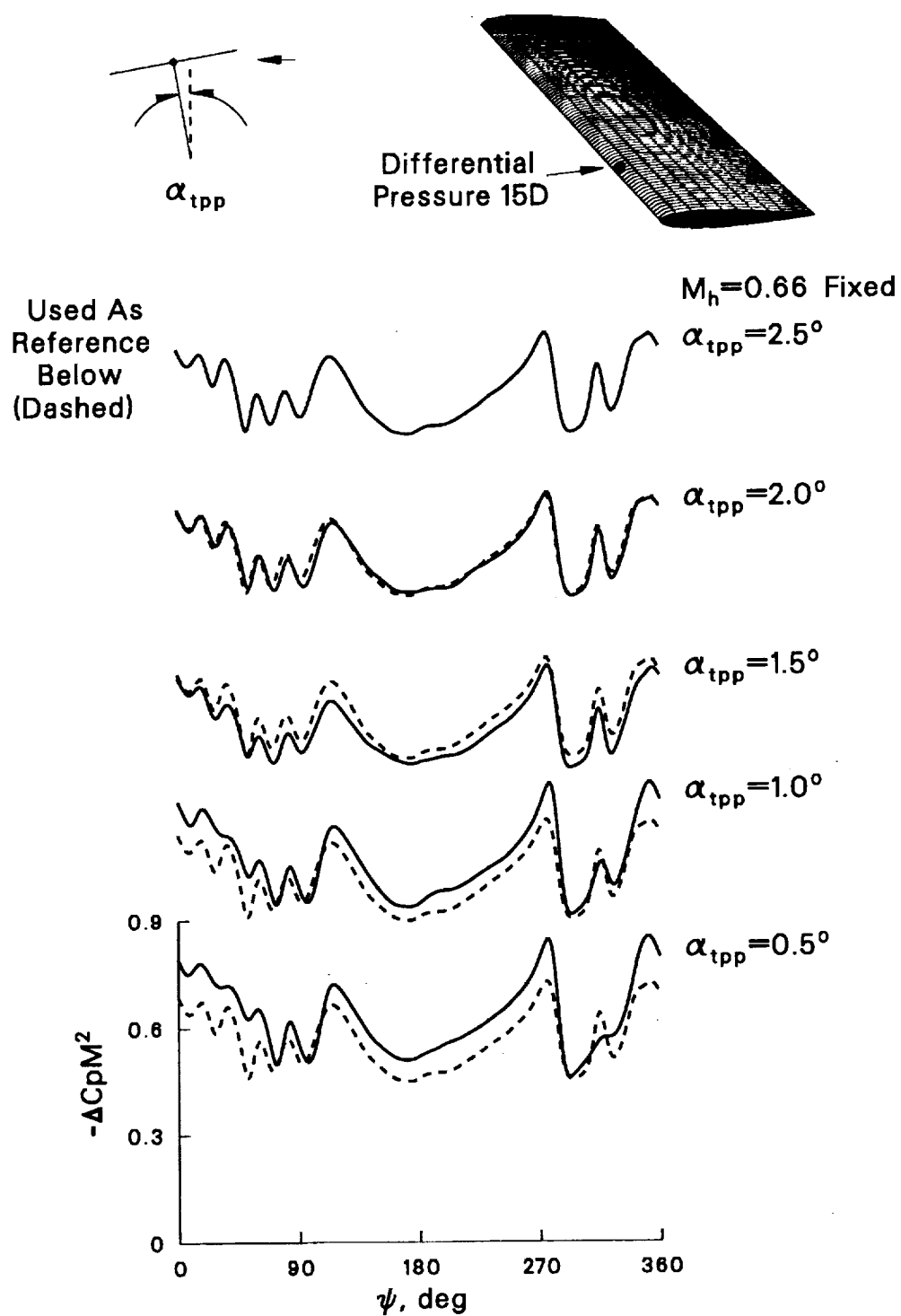


Figure 22. Periodic pressure response for range of tip-path plane angles (M_h fixed).

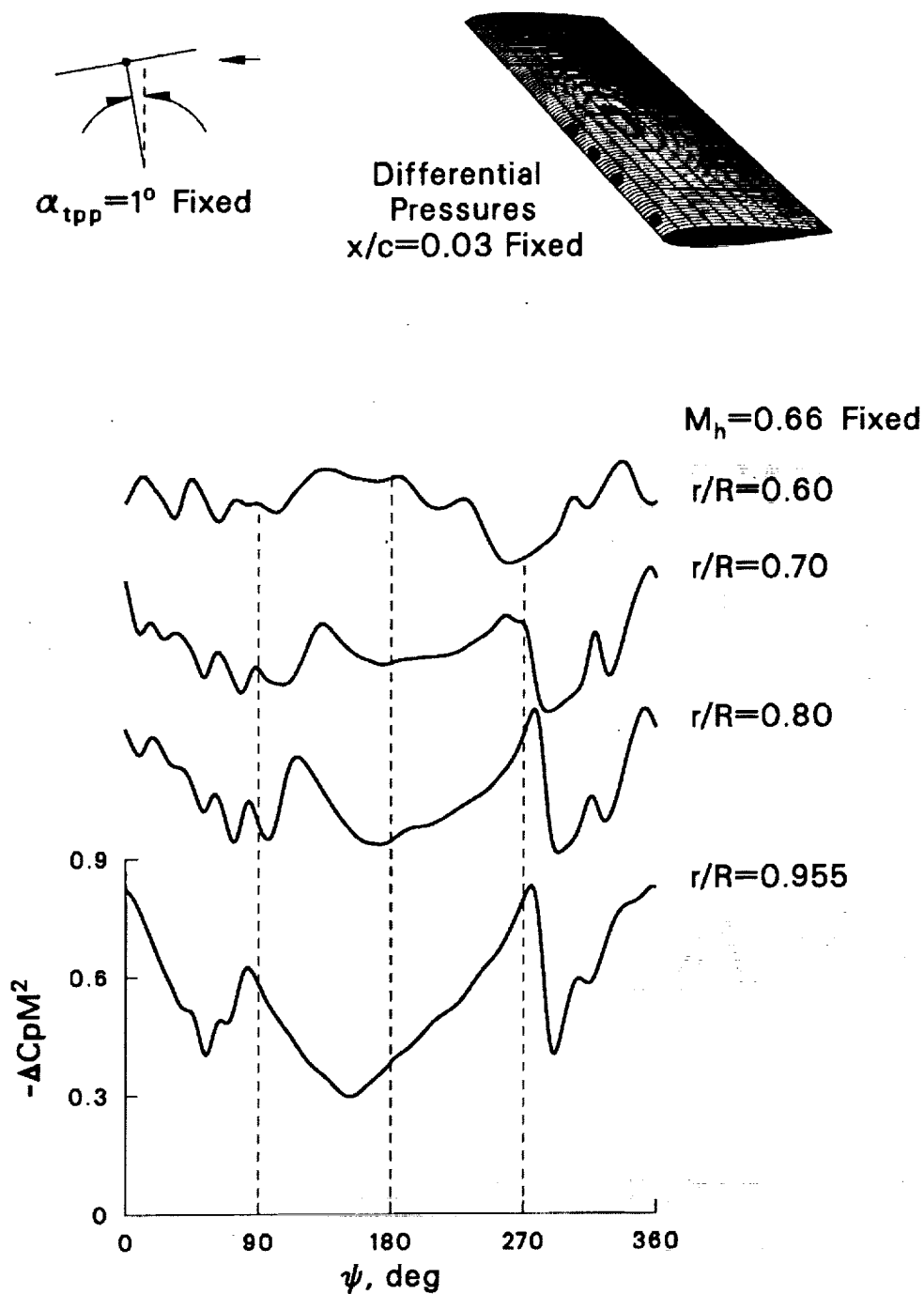


Figure 23. Periodic pressure response for range of radial stations (α_{tp} and M_h fixed).

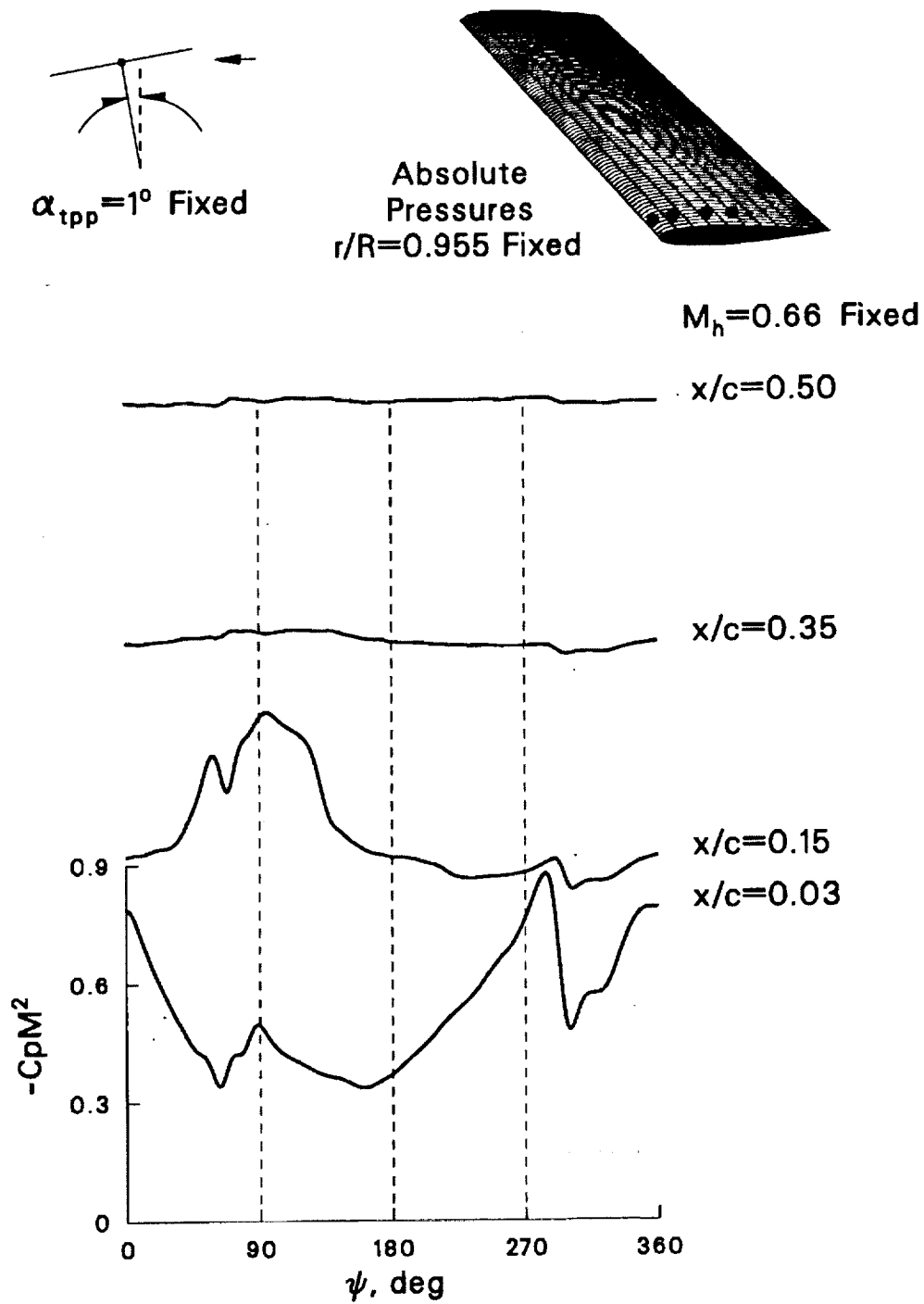


Figure 24. Periodic pressure response for range of chord stations (α_{tpp} and M_h fixed).

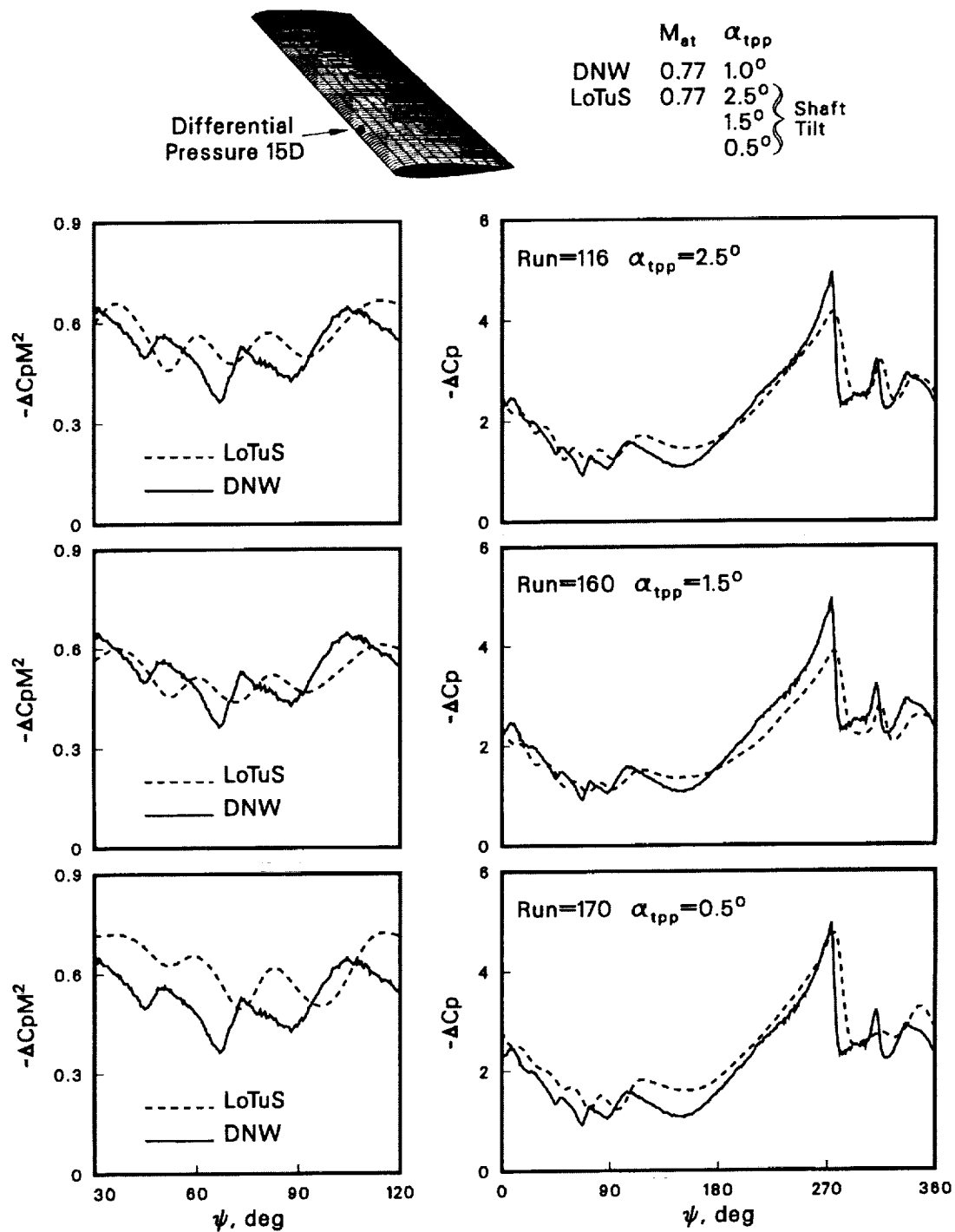


Figure 25. Blade pressure for several α_{tpp} compared with DNW test results.

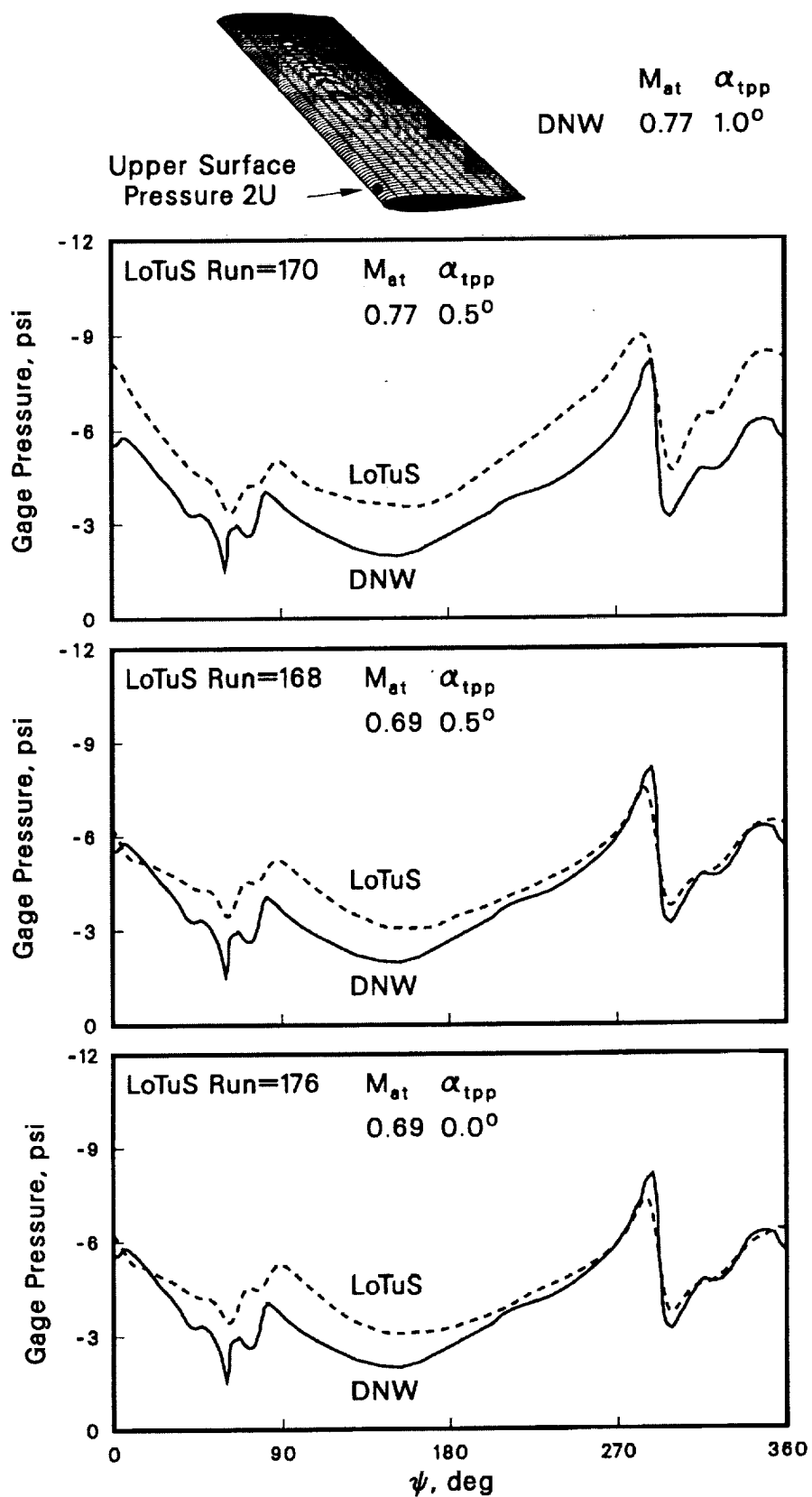


Figure 26. Pressure matching attempts at alternate values of α_{tpp} and M_{at} .

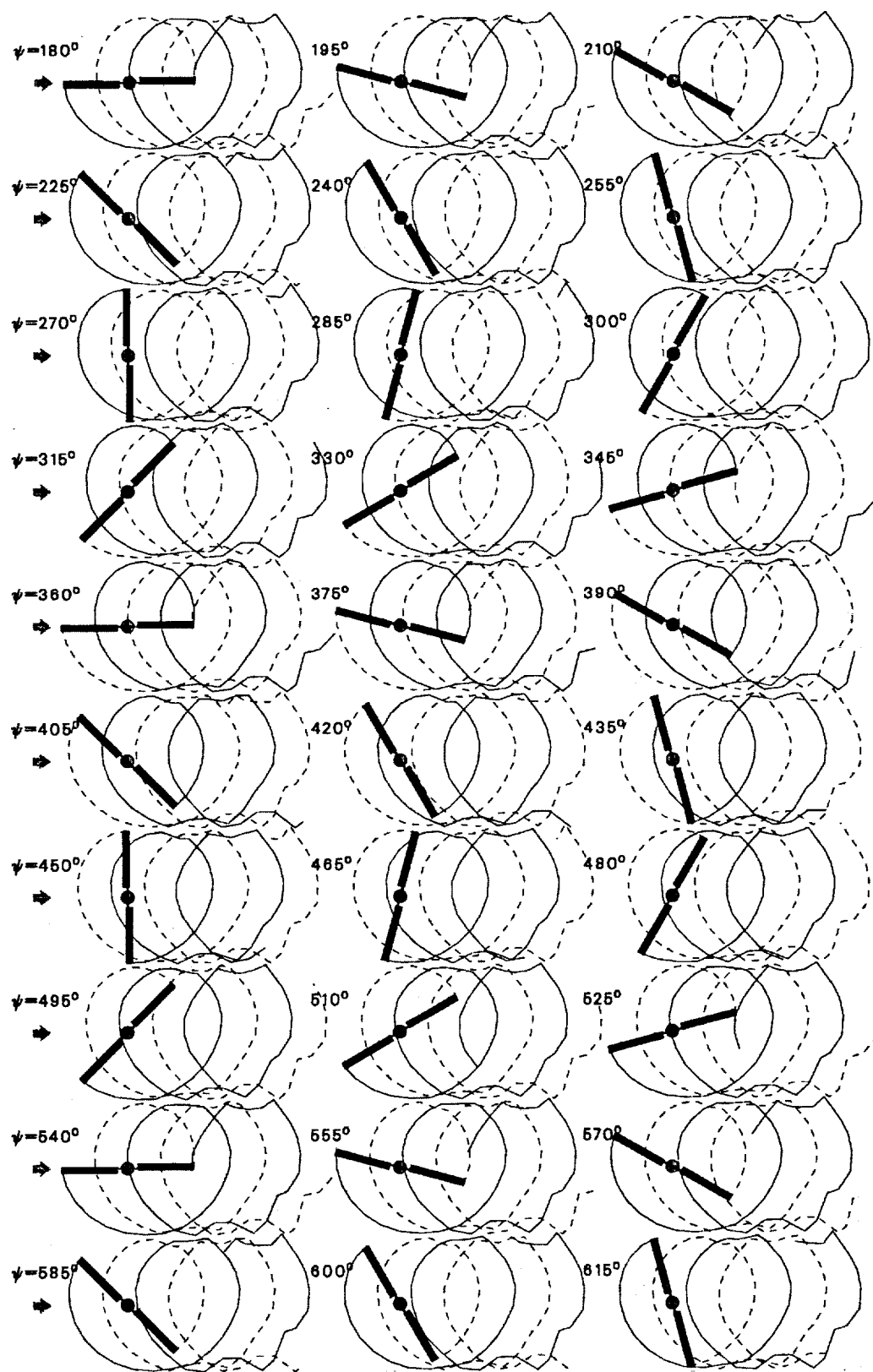


Figure 27. Calculated wake geometry for $C_T = 0.0054$, $M_{at} = 0.77$, $\mu = 0.16$, and $\alpha_{tp} = 1^\circ$.

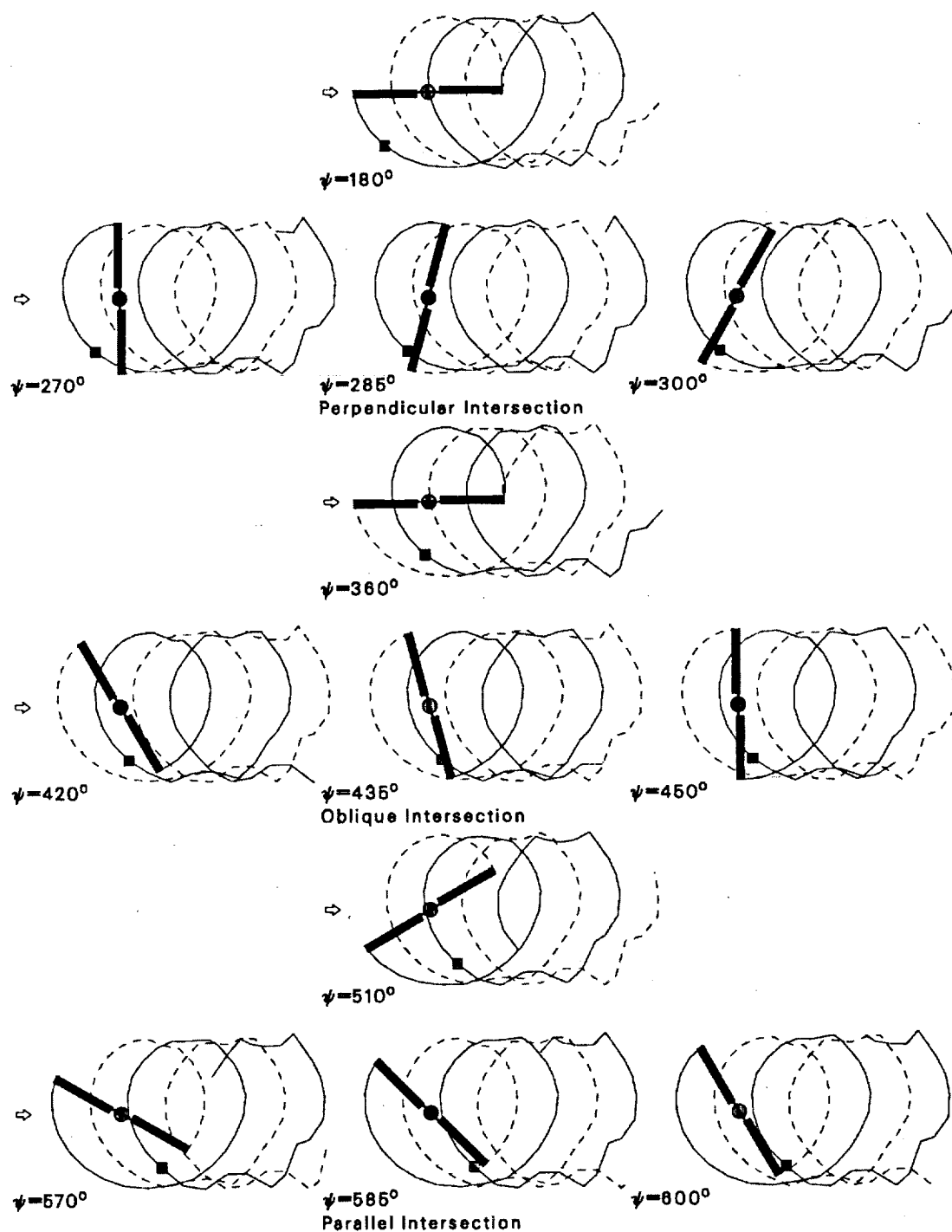


Figure 28. Calculated wake geometry showing critical vortex segment interactions.

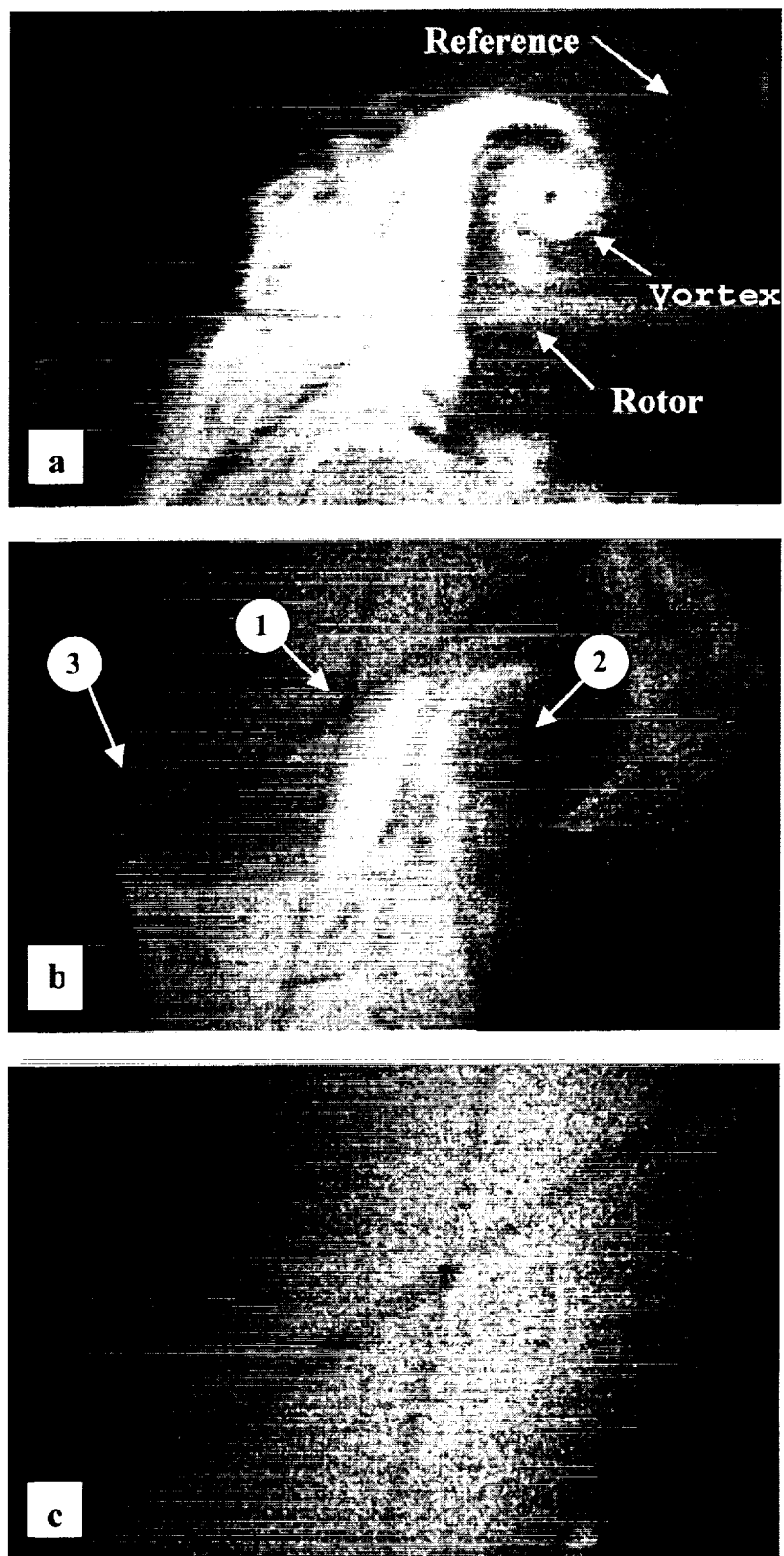


Figure 29. Wake visualizations with different concentrations of flow seeding. Particles introduced (a) upstream only, (b) both upstream and downstream, and (c) downstream only.

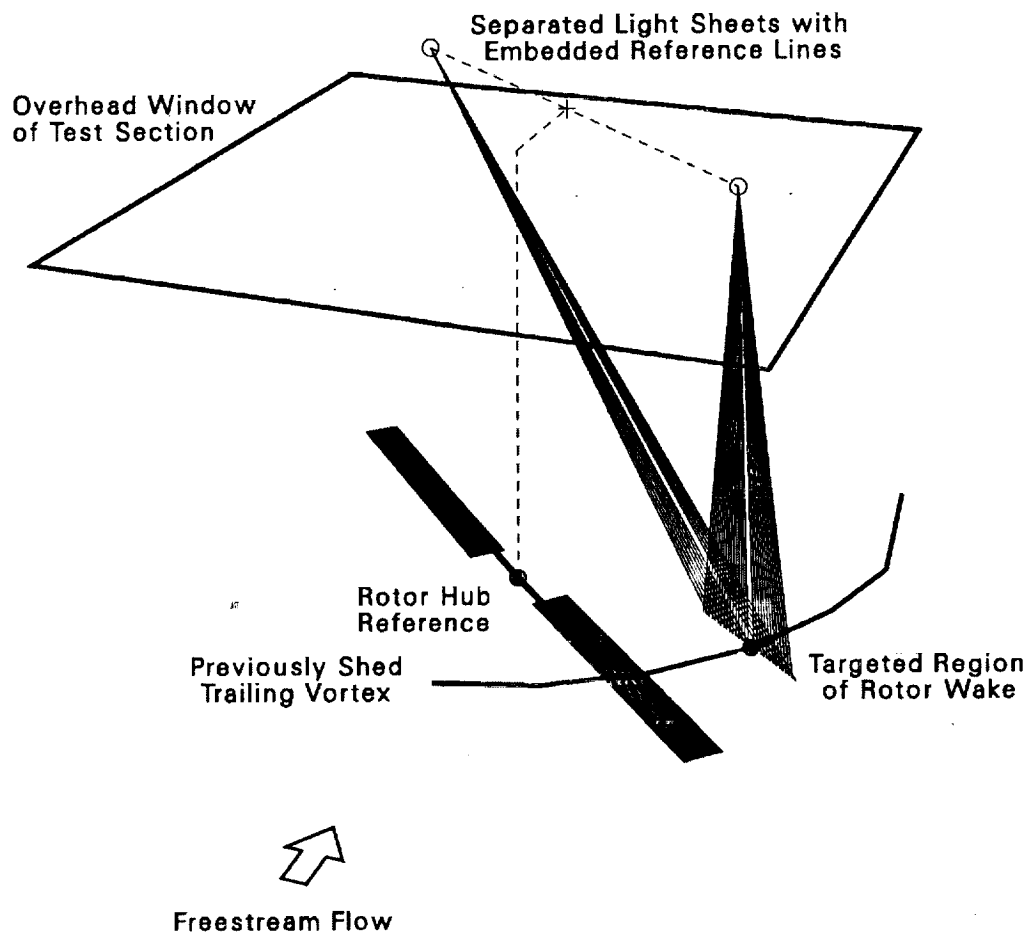


Figure 30. Laser-light sheet setup for determining coordinates of targeted region of flow.

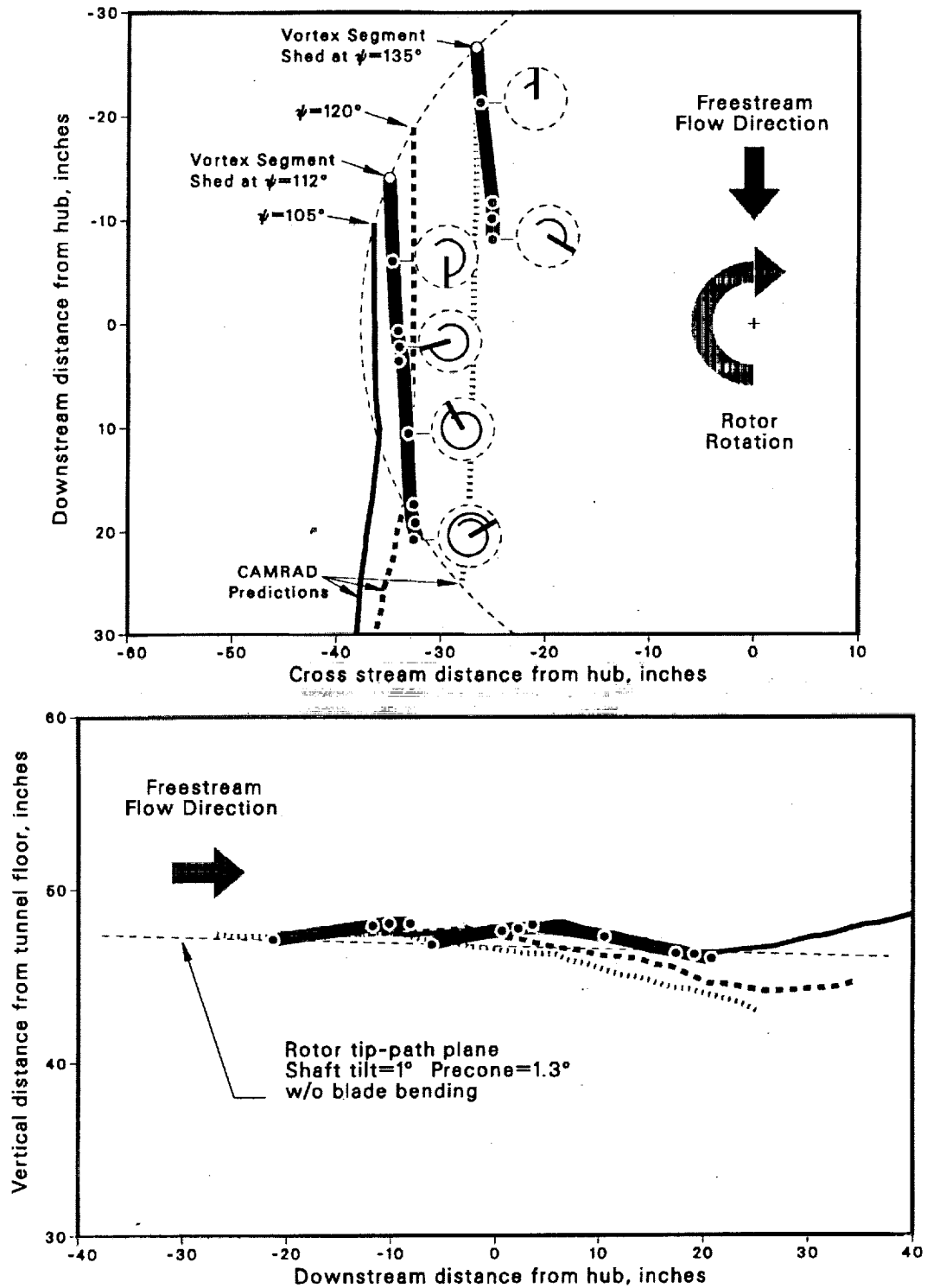


Figure 31. Trajectories of specific vortex segments within the rotor wake.

REPORT DOCUMENTATION PAGEForm Approved
OMB No. 0704-0188

Public reporting burden for this collection of information is estimated to average 1 hour per response, including the time for reviewing instructions, searching existing data sources, gathering and maintaining the data needed, and completing and reviewing the collection of information. Send comments regarding this burden estimate or any other aspect of this collection of information, including suggestions for reducing this burden, to Washington Headquarters Services, Directorate for Information Operations and Reports, 1215 Jefferson Davis Highway, Suite 1204, Arlington, VA 22202-4302, and to the Office of Management and Budget, Paperwork Reduction Project (0704-0188), Washington, DC 20503.

1. AGENCY USE ONLY (Leave blank)		2. REPORT DATE November 2000	3. REPORT TYPE AND DATES COVERED Technical Memorandum	
4. TITLE AND SUBTITLE Preliminary Study of a Model Rotor in Descent			5. FUNDING NUMBERS 581-10-12	
6. AUTHOR(S) K. W. McAlister, C. Tung, D. L. Sharpe, S. Huang, and E. M. Hendley				
7. PERFORMING ORGANIZATION NAME(S) AND ADDRESS(ES) Army/NASA Rotorcraft Division, Aeroflightdynamics Directorate (AMRDEC), U.S. Army Aviation and Missile Command, Ames Research Center, Moffett Field, CA 94035			8. PERFORMING ORGANIZATION REPORT NUMBER A-99V0024	
9. SPONSORING/MONITORING AGENCY NAME(S) AND ADDRESS(ES) National Aeronautics and Space Administration Washington, DC 20546-0001 and U.S. Army Aviation and Missile Command, Redstone Arsenal, AL 35898-5000			10. SPONSORING/MONITORING AGENCY REPORT NUMBER NASA/TM-2000-208785 AFDD/TR-99-A-001	
11. SUPPLEMENTARY NOTES Point of Contact: K. W. McAlister, Ames Research Center, MS 219-1, Moffett Field, CA 94035-1000 (650) 604-5892				
12a. DISTRIBUTION/AVAILABILITY STATEMENT Unclassified — Unlimited Subject Category 02 Availability: NASA CASI (301) 621-0390			12b. DISTRIBUTION CODE Distribution: Standard	
13. ABSTRACT (Maximum 200 words) <p>Within a program designed to develop experimental techniques for measuring the trajectory and structure of vortices trailing from the tips of rotor blades, the present preliminary study focuses on a method for quantifying the trajectory of the trailing vortex during descent flight conditions. This study also presents rotor loads and blade surface pressures for a range of tip-path plane angles and Mach numbers. Blade pressures near the leading edge and along the outer radius are compared with data obtained on the same model rotor, but in open jet facilities. A triangulation procedure based on two directable laser-light sheets, each containing an embedded reference, proved effective in defining the spatial coordinates of the trailing vortex. When interrogating a cross section of the flow that contains several trailing vortices, the greatest clarity was found to result when the flow is uniformly seeded. Surface pressure responses during blade-vortex interactions appeared equally sensitive near the leading edge and along the outer portion of the blade, but diminished rapidly as the distance along the blade chord increased. The pressure response was virtually independent of whether the tip-path plane angle was obtained through shaft tilt or cyclic pitch. Although the shape and frequency of the pressure perturbations on the advancing blade during blade-vortex interaction are similar to those obtained in open-jet facilities, the angle of the tip-path plane may need to be lower than the range covered in this study.</p>				
14. SUBJECT TERMS Rotor wake, Trailing vortex, Flow visualization; Model rotor, Helicopter descent			15. NUMBER OF PAGES 41	
			16. PRICE CODE A03	
17. SECURITY CLASSIFICATION OF REPORT Unclassified	18. SECURITY CLASSIFICATION OF THIS PAGE Unclassified	19. SECURITY CLASSIFICATION OF ABSTRACT	20. LIMITATION OF ABSTRACT	